

# A Novel THz Massive MIMO Beam Domain Channel Model for 6G Wireless Communication Systems

Jun Wang, *Student Member, IEEE*, Cheng-Xiang Wang , *Fellow, IEEE*, Jie Huang , *Member, IEEE*, Rui Feng , *Member, IEEE*, El-Hadi M. Aggoune , *Life Senior Member, IEEE*, and Yunfei Chen , *Senior Member, IEEE*

**Abstract**—In this paper, a three dimensional (3D) geometry based, stochastic model (GBSM) considering planar antenna array is firstly proposed for the sixth generation (6G) terahertz (THz) massive multiple-input multiple-output (MIMO) wireless communication systems. Then, a novel beam domain channel model (BDCM) is derived from the proposed GBSM based on the Fourier transform matrix from the spatial domain to the angle domain in horizontal and vertical directions simultaneously. The THz propagation characteristics, including non-negligible diffuse scattering and limited order of reflection, are considered in these two channel models. In addition, the proposed GBSM and BDCM can capture the spherical wavefront and spatial non-stationarity characteristics in massive MIMO channels by deriving steering vectors of near-field clusters and partly visible clusters, respectively. The angle-domain sparsity property of the BDCM can be observed, which helps reduce the complexity of the GBSM and improve the mathematical tractability. Typical statistical properties of the proposed GBSM and BDCM are derived and compared. The effects of the spherical wavefront on space-time-frequency correlation functions (STF-CFs) and channel capacity are also studied for the proposed GBSM and BDCM. The power leakage of the BDCM caused by the spherical wavefront and visible region (VR) is thoroughly analyzed. It is found that the statistical properties of the GBSM and BDCM

fit well and are considerably influenced by the spherical wavefront and VRs

**Index Terms**—6G, BDCM, GBSM, massive MIMO, THz band.

## I. INTRODUCTION

WITH the commercialization of the fifth generation (5G) mobile communications, the sixth generation (6G) has become a hot research field around the world [1], [2], [3], [4], [5]. The goal of 6G is to establish an ubiquitous mobile communication network with integrated communication, computing, sensing, and intelligence, so as to realize high-speed broadband communication with global coverage. The 6G vision is reaching a general consensus in the world [1], including global coverage, all spectra, full applications, and endogenous network security. In order to support the ultra-high data rate of 6G communications, higher frequency bands up to mmWave [6], [7], [8] and THz [9], [10], [11] need to be employed. The THz wireless communication system has a larger channel capacity due to the larger bandwidth compared with traditional bands. However, THz technologies are not widely used in 5G communications due to the high-cost of their devices. Recently, with the development of THz devices, THz transmission has been one of the key technologies for 6G.

Channel characterization and modeling are the foundations of system design, theoretical analysis, performance evaluation, and wireless systems optimization. Channel measurements and modeling for 5G wireless communication have been comprehensively surveyed [12]. However, the propagation channels of the THz waves have different characteristics compared with 5G scenarios due to their high frequency and short wavelength. The propagation characteristics of THz channels have been well investigated, such as high path loss [13], [14], [15], blockage effect [16], atmospheric attenuation [17], [18], and frequency domain non-stationarity [19]. THz indoor channel measurements were conducted in [13], where the path losses in different directions were evaluated to show the angular power spectral density (PSD). In [14], the frequency-dependence and distance-dependence were modeled based on channel measurements. Channel measurements and path loss characterization were conducted in indoor scenarios at 140 GHz and 220 GHz in [15]. The blockage effect was studied and proved to have a profound impact on the signal-to-interference-plus-noise ratio (SINR) [16]. In [17], authors developed an atmospheric attenuation prediction method between 0.1 THz and 100 THz. In [18],

Manuscript received 26 July 2022; revised 25 December 2022; accepted 11 February 2023. Date of publication 15 March 2023; date of current version 15 August 2023. This work was supported in part by the National Key R&D Program of China under Grant 2020YFB1804901, in part by the National Natural Science Foundation of China under Grants 61960206006 and 62271147, in part by the Key Technologies Research and Development Program of Jiangsu (Prospective and Key Technologies for Industry) under Grants BE2022067 and BE2022067-1, in part by the High Level Innovation and Entrepreneurial Doctor Introduction Program in Jiangsu under Grant JSSCBS20210082, in part by the EU H2020 RISE TESTBED2 Project under Grant 872172, in part by the Fellowship of China Postdoctoral Science Foundation under Grant 2021M690628, and in part by the Sensor Networks and Cellular Systems (SNCS) Research Center, University of Tabuk, under Grant 1444-154. The review of this article was coordinated by Prof. Arafat Al-Dweik. (*Corresponding author: Cheng-Xiang Wang.*)

Jun Wang, Cheng-Xiang Wang, and Jie Huang are with the National Mobile Communications Research Laboratory, School of Information Science and Engineering, Southeast University, Nanjing 210096, China, and also with the Purple Mountain Laboratories, Southeast University, Nanjing 211111, China (e-mail: jun.wang@seu.edu.cn; chxwang@seu.edu.cn; j\_huang@seu.edu.cn).

Rui Feng is with the Purple Mountain Laboratories, Southeast University, Nanjing 211111, China, and also with the School of Information Science and Engineering, Southeast University, Nanjing 210096, China (e-mail: fengxiurui604@163.com).

El-Hadi M. Aggoune is with the Sensor Networks and Cellular Systems Research Center, University of Tabuk, Tabuk 47315, Saudi Arabia (e-mail: haggoune.snscs@ut.edu.sa).

Yunfei Chen is with the Department of Engineering, University of Durham, Durham DH1 3LE, U.K. (e-mail: yunfei.chen@durham.ac.uk).

Digital Object Identifier 10.1109/TVT.2023.3257490

the authors developed a unified molecular absorption model based on the line-by-line integration method, and an in-depth analysis on the THz absorption was carried out based on the developed propagation model. The non-stationarity caused by large bandwidth was studied in [19]. In addition, the diffuse scattering in THz band was investigated in [20], [21], [22]. The channel measurements [21] and theoretical analysis [22] showed that the diffuse scattering is indispensable in THz channel modeling.

Because of the unique channel characteristics, traditional channel models cannot support the THz frequency band. The standard channel models proposed by the third generation partnership project (3GPP) [23] and the International Telecommunication Union (ITU) [24] can only support frequencies up to 100 GHz. Researchers have conducted in-depth studies on THz channel modeling and proposed many THz channel models. For example, in [25], the authors proposed a stochastic 300 GHz indoor channel model. This channel model considered amplitude, phase, and spatial channel information and was verified by ray tracing simulation in an office environment. In [26], the authors investigated spatial and temporal channel properties at 300 GHz in an indoor environment. The root mean squared (RMS) angular and delay spreads were determined by ray tracing simulation. In [27], a multi-ray propagation model incorporating the line-of-sight (LoS), reflected, scattered, and diffracted paths was proposed and validated by the experimental measurements. In [28], a hybrid modeling approach which combines the deterministic and stochastic modeling methods was proposed. This channel model considered three propagation mechanisms, including LoS, reflection, and scattering.

On the other hand, in recent years, multiple-input multiple-output (MIMO) technology has been utilized in THz research to compensate for the high path loss [29], [30], [31], [32], [33]. The scale of MIMO will expand to ultra-massive MIMO in 6G [34], [35], [36]. The increase of antenna size will also produce many unique channel characteristics, such as spherical wavefront and spatial non-stationarity. From the perspective of large antenna arrays, the boundary of near- and far-fields is defined as the Rayleigh distance calculated by  $R = \frac{2L^2}{\lambda}$ , where  $L$  represents the dimension of the array and  $\lambda$  is the wavelength. With the increase of array size, the Rayleigh distance increases greatly at the same frequency, and the distance between scatterers and the antenna array no longer meets the far-field condition. In this case, the spherical wavefront needs to be considered. In addition, different scatterers may be observed by different elements of the array, which will cause the spatial non-stationarity along the array axis. MIMO channel models have evolved with the continuous development of MIMO technology [23], [24], [37], [38], [39], [40]. MIMO channel characteristics and channel models have been extensively studied. So far, the most widely used 3GPP TR 38.901 [23] channel model supported massive MIMO. It gave the detailed channel parameters of various scenarios. However, it can only support frequency bands below 100 GHz. In [38], the authors proposed the ultra-massive MIMO channel model for THz band considering space-time-frequency (STF) non-stationarity. In [39], the authors proposed a general three dimensional (3D) non-stationary wireless channel model for 5G

and beyond. It presented a general modeling framework that can include a variety of simplified channel models as special cases. In [40], a more pervasive 6G channel model for all frequency bands and all scenarios was proposed. This channel model could be simplified to typical 5G channel models by flexible parameter adjustments.

Apart from the geometry based stochastic model (GBSM), MIMO channel can be characterized by dividing beams at the transmitter (Tx) side and receiver (Rx) side. This is called the beam domain channel model (BDCM) [44], [45], [46]. By sampling the propagation environment in the spatial domain, BDCMs characterize the power coupling between transmit and receive beams. Compared with the traditional GBSM, BDCM has the advantage that the channel transmission matrix is sparse in the delay-angular domain at mmWave and THz bands [47]. This allows some algorithms, such as compressed sensing [48], to reduce the complexity of system optimization or performance evaluation. The BDCM also provides an easier way of beamforming for potential applications of THz technologies, such as ultra-massive MIMO [34], [35] and reconfigurable intelligent surfaces (RIS) [41], [42], [43]. An intermediate virtual channel representation method was proposed in [44]. It captured the essence of physical modeling and provided a simple geometric explanation of the scattering environment. In [45], the authors studied a fully correlated channel matrix and provided a BDCM, where the channel gains are independent of sub-carriers. Based on this BDCM, a beam division multiple access (BDMA) transmission scheme was proposed. In [46], the authors introduced a physically motivated BDCM and proposed BDMA with per-beam synchronization in time and frequency domains for wideband massive MIMO transmission.

However, the BDCMs in the literature assumed that all the scatterers are located in far-field regions. The spherical wavefront was only studied in GBSMs, but how to describe the spherical wavefront and birth-death process in BDCMs remains a challenge. Recently, several BDCMs for B5G massive MIMO were proposed in [49], [50]. These BDCMs consider spherical wavefront but could not support THz band. To fill these gaps, in this paper, a novel 3D THz BDCM considering the spherical wavefront and partly visible clusters is proposed. Compared with the GBSM for THz massive MIMO channels in [38], our new BDCM simplifies the complexity of the GBSM by having a sparse channel matrix. Different from the BDCMs in [44], [45], [46], our new BDCM can support specific 6G THz massive MIMO channel characteristics. The main contributions and novelties of this paper are as follows.

- 1) A general GBSM considering THz scattering and reflecting characteristics is proposed for 6G THz massive MIMO wireless communication systems. The spherical wavefront and spatial non-stationarity of THz massive MIMO channels are characterized by calculating steering vectors for near-field clusters and partly visible clusters, respectively.
- 2) Then, a THz massive MIMO BDCM is proposed from the the GBSM by using a Fourier transform matrix from the spatial domain to angle domain. It is the first BDCM considering both spherical wavefront and spatial non-stationarity characteristics for THz massive MIMO

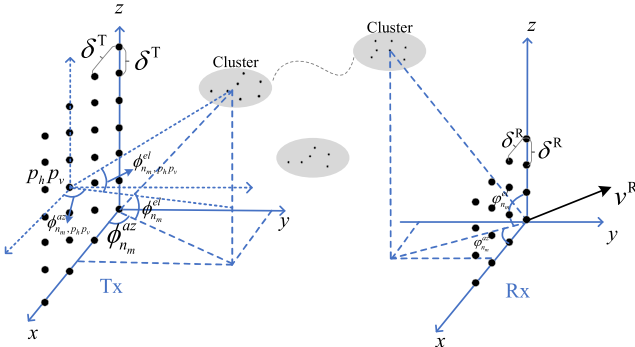


Fig. 1. Diagram of the scattering propagation.

communications. The BDCM shows evident sparsity properties in the angle domain, which will help to reduce the complexity of the GBSM and improve the mathematical tractability.

- 3) The statistical properties of the proposed GBSM and BDCM are derived, simulated, and compared, such as the space-time-frequency correlation functions (STF-CFs) and channel capacities. The derivation and simulation results show good agreement between these two channel models. In addition, The power leakage of the BDCM is also analyzed. It is found that the near-field spherical wavefront and VRs have great impact on the statistical properties of the proposed GBSM and BDCM.

The remainder of this paper is organized as follows. In Section II, the THz GBSM is described in details. Different steering vectors for three types of clusters are derived. In Section III, the THz BDCM is proposed based on the GBSM. The statistical properties of the proposed GBSM and BDCM are derived in Section IV. In Section V, different statistical properties of the BDCM are simulated and compared with GBSM. Finally, conclusions are drawn in Section VI.

## II. A GENERAL 3D NON-STATIONARY THz GBSM

The diagram of a THz wireless communication system is shown in Fig. 1. At the base station (BS) side, the transmitter (Tx) employs a large-scale uniform planar array (UPA). At the user side, the receiver (Rx) is also equipped with UPA, but the antenna number is smaller. Without loss of generality, the large UPA at Tx is aligned on the  $x$ - $z$  plane and has a dimension of  $P = P_h \times P_v$ . The UPA at Rx is aligned on the  $x$ - $z$  plane and has a dimension of  $Q = Q_h \times Q_v$ , where  $P_h$  ( $Q_h$ ) and  $P_v$  ( $Q_v$ ) are the numbers of antenna elements in horizontal and vertical dimensions at Tx (Rx), respectively. Note that the  $p$ th Tx antenna element is located at the  $p_h$ th row and  $p_v$ th column. They have the relationship  $p = (p_h - 1)P_v + p_v$ . At Rx side, we have  $q = (q_h - 1)Q_v + q_v$ , where the  $q$ th Tx antenna element is located at the  $q_h$ th row and  $q_v$ th column. The spacings between adjacent elements at Tx and Rx are denoted as  $\delta^T$  and  $\delta^R$ , respectively. The main parameters are defined in Table I. Note that, in the global coordinate system, the antenna position of Rx can be transmitted into the  $x$ - $z$  plane by using the coordinate transformation method discussed in [23].

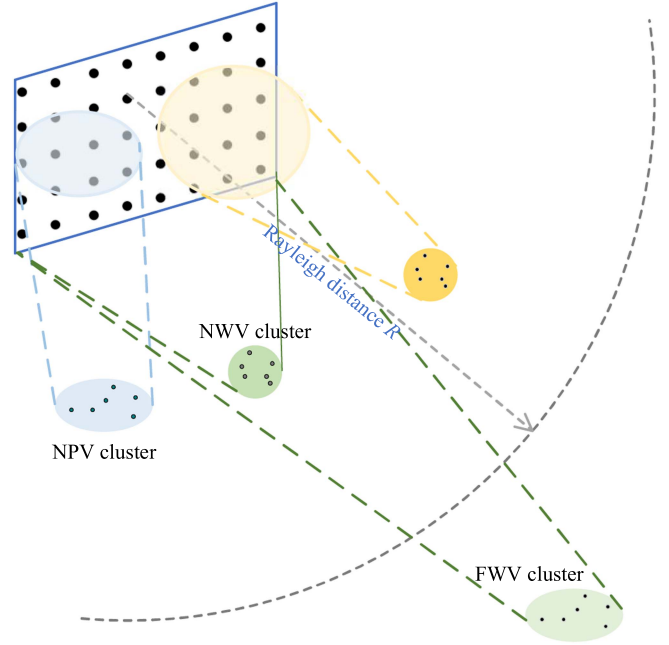


Fig. 2. Multi-bounce scattering propagation.

Considering the large aperture size of the array, clusters in massive MIMO channels can be classified as far-field clusters and near-field clusters. Birth-death process along the array and visible region are two methods to capture the non-stationarity. In this paper, these clusters are also classified as wholly visible clusters and partly visible clusters. The far-field clusters are normally far from the antenna array and considered as wholly visible clusters. In order to distinguish wholly/partly visible clusters from far/near-field, in this paper, we classify all clusters into three types, i.e., far-field wholly visible (FWV) clusters, near-field wholly visible (NWV) clusters, and near-field partly visible (NPV) clusters. As shown in Fig. 2, the clusters whose distances to the array are larger than the Rayleigh distance are considered as FWV. The clusters located in the near-field region but visible to all antenna elements are called NWV. Also, the clusters located in the near-field region but only visible to part of antenna elements are considered as NPV. Considering the actual application scenario, we assume that the large UPA is only equipped at Tx, so that the spherical wavefront and partly visible analysis are not considered at the Rx side. Thus, the CTF from the  $p$ th transmit antenna to the  $q$ th receive antenna can be expressed as

$$h_{p,q}(t, f) = h_{p,q}^{\text{FWV}}(t, f) + h_{p,q}^{\text{NWV}}(t, f) + h_{p,q}^{\text{NPV}}(t, f) \quad (1)$$

where  $h_{p,q}^{\text{FWV}}(t, f)$ ,  $h_{p,q}^{\text{NWV}}(t, f)$ , and  $h_{p,q}^{\text{NPV}}(t, f)$  are the FWV, NWV, and NPV components, respectively. They are given by

$$h_{p,q}^{\text{FWV}}(t, f) = \sum_{n \in \mathcal{B}_{\text{FWV}}} \sum_{m=1}^{M_n} \beta_{m_n} \cdot e^{j[2\pi(\nu_{m_n}t - f\tau_{m_n}) + \Phi_{m_n}]} \cdot \psi_p^{\text{T,FWV}}(\phi_{m_n}^{\text{az}}, \phi_{m_n}^{\text{el}}) \cdot \psi_q^{\text{R}}(\varphi_{m_n}^{\text{az}}, \varphi_{m_n}^{\text{el}}) \quad (2)$$

TABLE I  
DEFINITIONS OF MAIN PARAMETERS FOR THE PROPOSED THZ CHANNEL MODEL

Parameters	Definitions
$\delta^T, \delta^R$	Inter-element spacings of Tx and Rx, respectively
$D$	Distance between the center of Tx and Rx at initial time
$\mathcal{B}_{\text{FWV}}, \mathcal{B}_{\text{NWV}}, \mathcal{B}_{\text{NPV}}$	FWV, NWV, and NPV cluster index sets, respectively
$\phi_{m_n}^{\text{az}}, \phi_{m_n}^{\text{el}}$	Azimuth and elevation angles of the $m$ th path in the $n$ th cluster at the Tx side
$\phi_{m_n, p_h, p_v}^{\text{az}}, \phi_{m_n, p_h, p_v}^{\text{el}}$	Azimuth and elevation angles of the $m$ th path in the $n$ th cluster for the $p_h$ th row and the $p_v$ th column element
$\varphi_{m_n}^{\text{az}}, \varphi_{m_n}^{\text{el}}$	Azimuth and elevation angles of the $m$ th path in the $n$ th cluster at the Rx side
$v^T, v^R$	Velocities of Tx and Rx

$$h_{p,q}^{\text{NWV}}(t, f) = \sum_{n \in \mathcal{B}_{\text{NWV}}} \sum_{m=1}^{M_n} \beta_{m_n} \cdot e^{j[2\pi(\nu_{m_n} t - f \tau_{m_n}) + \Phi_{m_n}]} \cdot \psi_p^{\text{T, NWV}}(\phi_{m_n}^{\text{az}}, \phi_{m_n}^{\text{el}}) \cdot \psi_q^{\text{R}}(\varphi_{m_n}^{\text{az}}, \varphi_{m_n}^{\text{el}}) \quad (3)$$

$$h_{p,q}^{\text{NPV}}(t, f) = \sum_{n \in \mathcal{B}_{\text{NPV}}} \sum_{m=1}^{M_n} \beta_{m_n} \cdot \xi_{pq, nm} \cdot e^{j[2\pi(\nu_{m_n} t - f \tau_{m_n}) + \Phi_{m_n}]} \cdot \psi_p^{\text{T, NPV}}(\phi_{m_n}^{\text{az}}, \phi_{m_n}^{\text{el}}) \cdot \psi_q^{\text{R}}(\varphi_{m_n}^{\text{az}}, \varphi_{m_n}^{\text{el}}) \quad (4)$$

where  $n$  and  $m$  are the cluster and ray indices, respectively.  $\mathcal{B}_{\text{FWV}}$ ,  $\mathcal{B}_{\text{NWV}}$ , and  $\mathcal{B}_{\text{NPV}}$  denote index sets of FWV clusters, NWV clusters, and NPV clusters, respectively. The category of a cluster can be distinguished by its index  $n$ . For all three types of clusters, the total number of rays in the  $n$ th cluster is denoted as  $M_n$ . The path gain is defined as  $\beta_{m_n} = \sqrt{\frac{K_R}{K_R+1}}$  for  $n = 0$  and  $\beta_{m_n} = \sqrt{\frac{P_{n,m}}{K_R+1}}$  for  $n = 1, \dots, N$ , where  $K_R$  denotes the Rician factor, and  $P_{n,m}$  represents power of the  $m$ th ray in the  $n$ th cluster. For NPV clusters in (4), the channel gain is modified by path visibility factor  $\xi_{pq, nm}$ . The Doppler frequency is calculated by  $\nu_{m_n} = f_m \cdot \cos(\varphi_{m_n}^{\text{el}}) \cos(\varphi_{m_n}^{\text{az}} - \alpha)$  where  $f_m = v/\lambda$ . Furthermore,  $\tau_{m_n}$  and  $\Phi_{m_n}$  account for delay and random phase, respectively. The generation method of parameters was introduced in [38], including the delay, phase, and power of each ray. This method considered THz unique propagation mechanisms, including limited order of reflections and non-ignorable diffuse scattering. Different from the channel transmission matrix in [38], this work classifies all the clusters into three categories and calculate the steering vector for antenna arrays of each in this paper. The mathematical expression of channel transmission function in this paper is more suitable to be transformed to the beam domain. In addition to the spatial non-stationarity caused by massive MIMO, the channel model [38] also considers the time domain non-stationarity caused by long traveling path and the frequency domain non-stationarity. Therefore, by using the same generating and updating methods of channel parameters, the GBSM and BDCM in this paper have the ability to support vehicular applications including the high-speed propagation scenarios. In (2)–(4), the phase differences of antenna elements at Tx side for three types of clusters are different and denotes as  $\psi^{\text{T, FWV}}$ ,  $\psi^{\text{T, NWV}}$ , and  $\psi^{\text{T, NPV}}$ . The phase difference at Rx side is denoted as  $\psi^{\text{R}}$  and calculated by

$$\psi_q^{\text{R}}(\varphi_{m_n}^{\text{az}}, \varphi_{m_n}^{\text{el}}) = e^{j \frac{2\pi}{\lambda} [(q_n - 1) \delta^T \cos \varphi_{m_n}^{\text{el}} \sin \varphi_{m_n}^{\text{az}} + (q_v - 1) \delta^T \sin \varphi_{m_n}^{\text{el}}]}. \quad (5)$$

For FWV clusters, the angles of departure for all antenna elements are the same. The phase difference of  $p$ th element can be calculated by

$$\psi_p^{\text{T, NWV}}(\phi_{m_n}^{\text{az}}, \phi_{m_n}^{\text{el}}) = e^{j \frac{2\pi}{\lambda} [(p_h - 1) \delta^T \cos \phi_{m_n}^{\text{el}} \sin \phi_{m_n}^{\text{az}} + (p_v - 1) \delta^T \sin \phi_{m_n}^{\text{el}}]}. \quad (6)$$

For NWV and NPV clusters, we calculate the phase difference based on the spherical wavefront to obtain the steering vector, and then, we introduce use ray visibility matrix to modify the influence of VRs. We define  $\rho_n$  as the ratio of the distance from the cluster to the reference antenna and the Rayleigh distance. It can be calculated by

$$\rho_n = \frac{d_n^T}{R} = \frac{d_n^T \lambda}{2(P_h^2 + P_v^2) \delta^T} \quad (7)$$

where  $d_n^T$  is the the distance from the cluster to the reference antenna,  $d_n = 2\rho_n(P_h^2 + P_v^2) \delta^T / \lambda$ . The phase difference of  $p$ th element of NWV and NPV clusters can be calculated by

$$\psi_p^{\text{T, NWV/NPV}}(\phi_{m_n, p_h, p_v}^{\text{az}}, \phi_{m_n, p_h, p_v}^{\text{el}}) = e^{j \frac{2\pi}{\lambda} [(p_h - 1) \delta^T \cos \phi_{m_n, p_h, p_v}^{\text{el}} \sin \phi_{m_n, p_h, p_v}^{\text{az}} + (p_v - 1) \delta^T \sin \phi_{m_n, p_h, p_v}^{\text{el}}]} \quad (8)$$

where  $\phi_{m_n, p_h, p_v}^{\text{el/az}}$  accounts for the elevation/azimuth angles from the  $p_h$ th row and  $p_v$ th column element to the  $m$ th ray in the  $n$ th cluster. Due to the spherical wavefront caused by large-scale antenna array, the angle of scatterers in the near-field range seen by each antenna element is different. The angles  $\phi_{m_n, p_h, p_v}^{\text{el}}$  and  $\phi_{m_n, p_h, p_v}^{\text{az}}$  can be calculated by  $d_{m_n}$ ,  $\phi_{m_n}^{\text{el}}$ , and  $\phi_{m_n}^{\text{az}}$  as

$$\cos \phi_{m_n, p_h, p_v}^{\text{el}} \sin \phi_{m_n, p_h, p_v}^{\text{az}} = \frac{d_{m_n} \cos \phi_{m_n}^{\text{el}} \sin \phi_{m_n}^{\text{az}}}{\sqrt{a^2 + b^2 + d_{m_n}^2 - 2bd_{m_n} \cos \phi_{m_n}^{\text{el}} \cos \phi_{m_n}^{\text{az}} - 2ad_{m_n} \sin \phi_{m_n}^{\text{el}}}} \quad (9)$$

$$\sin \phi_{m_n, p_h, p_v}^{\text{el}} = \frac{-a + d_{m_n} \sin \phi_{m_n}^{\text{el}}}{\sqrt{a^2 + b^2 + d_{m_n}^2 - 2bd_{m_n} \cos \phi_{m_n}^{\text{el}} \cos \phi_{m_n}^{\text{az}} - 2ad_{m_n} \sin \phi_{m_n}^{\text{el}}}} \quad (10)$$

where  $a = (p_v - 1) \delta^T$  and  $b = (p_h - 1) \delta^T$ . The detailed derivations of (9) and (10) are shown in Appendix A.

For the convenience of analyzing transmission problems, the CTF is written as a  $P \times Q$  matrix, i.e.,

$$\mathbf{H}(t, f) = \mathbf{H}^{\text{FWV}}(t, f) + \mathbf{H}^{\text{NWV}}(t, f) + \mathbf{H}^{\text{NPV}}(t, f) \quad (11)$$

with

$$\mathbf{H}^{\text{FWV}}(t, f) = \sum_{n \in \mathcal{B}_{\text{FWV}}} \sum_{m=1}^{M_n} \beta_{m_n} \cdot e^{j[2\pi(\nu_{m_n} t - f \tau_{m_n}) + \Phi_{m_n}]}$$

$$\mathbf{V}(\varphi_{m_n}^{\text{az}}, \varphi_{m_n}^{\text{el}}) \mathbf{U}(\phi_{m_n}^{\text{az}}, \phi_{m_n}^{\text{el}}) \quad (12)$$

$$\mathbf{H}^{\text{NWV}}(t, f) = \sum_{n \in \mathcal{B}_{\text{NWV}}} \sum_{m=1}^{M_n} \beta_{m_n} \cdot e^{j[2\pi(\nu_{m_n} t - f \tau_{m_n}) + \Phi_{m_n}]}$$

$$\mathbf{V}(\varphi_{m_n}^{\text{az}}, \varphi_{m_n}^{\text{el}}) \mathbf{U}_N(\phi_{m_n}^{\text{az}}, \phi_{m_n}^{\text{el}}) \quad (13)$$

$$\mathbf{H}^{\text{NPV}}(t, f) = \sum_{n \in \mathcal{B}_{\text{NPV}}} \sum_{m=1}^{M_n} \beta_{m_n} \cdot e^{j[2\pi(\nu_{m_n} t - f \tau_{m_n}) + \Phi_{m_n}]}$$

$$\mathbf{V}(\varphi_{m_n}^{\text{az}}, \varphi_{m_n}^{\text{el}}) \hat{\mathbf{U}}_N(\phi_{m_n}^{\text{az}}, \phi_{m_n}^{\text{el}}) \quad (14)$$

where  $\mathbf{U}(\phi_{m_n}^{\text{az}}, \phi_{m_n}^{\text{el}})$  and  $\mathbf{V}(\varphi_{m_n}^{\text{az}}, \varphi_{m_n}^{\text{el}})$  can be expressed by

$$\mathbf{U}(\phi_{m_n}^{\text{az}}, \phi_{m_n}^{\text{el}}) = [\mathbf{b}(\theta_{m_n}^{\text{el}}) \otimes \mathbf{a}(\theta_{m_n}^{\text{az}})]^T \quad (15)$$

$$\mathbf{V}(\varphi_{m_n}^{\text{az}}, \varphi_{m_n}^{\text{el}}) = [\mathbf{b}(\vartheta_{m_n}^{\text{el}}) \otimes \mathbf{a}(\vartheta_{m_n}^{\text{az}})]^T \quad (16)$$

$$\mathbf{a}(\theta) = [1, e^{j2\pi\theta}, \dots, e^{j2\pi(P_h-1)\theta}]^T \quad (17)$$

$$\mathbf{b}(\theta) = [1, e^{j2\pi\theta}, \dots, e^{j2\pi(P_v-1)\theta}]^T \quad (18)$$

where  $\mathbf{a}(\theta)$  and  $\mathbf{b}(\theta)$  are steering vectors in azimuth and elevation, respectively. The elevation and azimuth directions associate with the  $m$ th ray in the  $n$ th cluster at Tx side  $\theta_{m_n}^{\text{el}} = 0.5 \sin \phi_{m_n}^{\text{el}}$  and  $\theta_{m_n}^{\text{az}} = 0.5 \cos \phi_{m_n}^{\text{el}} \sin \phi_{m_n}^{\text{az}}$ . At Rx side,  $\vartheta_{m_n}^{\text{el}} = 0.5 \sin \varphi_{m_n}^{\text{el}}$  and  $\vartheta_{m_n}^{\text{az}} = 0.5 \cos \varphi_{m_n}^{\text{el}} \sin \varphi_{m_n}^{\text{az}}$ .

For near-field clusters, the steering vector  $\mathbf{U}_N(\phi_{m_n}^{\text{az}}, \phi_{m_n}^{\text{el}})$  cannot be calculated by the Kronecker product of horizontal and vertical steering vectors directly. It is because the phase difference of the  $p$ th element is affected by the horizontal and vertical index simultaneously. The phase difference of the  $p$ th element can be written as  $e^{j2\pi[(p_v-1) \sin \phi_{m_n}^{\text{el}} \sin \phi_{m_n}^{\text{az}} + (p_h-1) \cos \phi_{m_n}^{\text{el}} \sin \phi_{m_n}^{\text{az}}]}$ .

To solve this problem, we need a reasonable approximation without losing the characteristics of spherical wave. The simplified and approximated  $\cos \phi_{m_n}^{\text{el}} \sin \phi_{m_n}^{\text{az}}$  and  $\sin \phi_{m_n}^{\text{el}} \sin \phi_{m_n}^{\text{az}}$  are calculated as

$$\begin{aligned} \cos \phi_{m_n}^{\text{el}} \sin \phi_{m_n}^{\text{az}} &\approx \frac{d_{m_n} \cos \phi_{m_n}^{\text{el}} \sin \phi_{m_n}^{\text{az}}}{d_{m_n} - b} \\ &= \frac{d_{m_n} \cos \phi_{m_n}^{\text{el}} \sin \phi_{m_n}^{\text{az}}}{d_{m_n} - (p_v - 1)\delta^T} \quad (19) \\ \sin \phi_{m_n}^{\text{el}} \sin \phi_{m_n}^{\text{az}} &\approx \frac{-a + d_{m_n} \sin \phi_{m_n}^{\text{el}}}{d_{m_n} - a} \\ &= \frac{-(p_h - 1)\delta^T + d_{m_n} \sin \phi_{m_n}^{\text{el}}}{d_{m_n} - (p_h - 1)\delta^T}. \quad (20) \end{aligned}$$

The necessary condition for the approximations is that the distance from the cluster to the array  $d_{m_n}$  is much larger than  $a$  and  $b$ . This condition is satisfied when  $\rho_n > 0.1$ . Then, the steering vector for near-field clusters  $\mathbf{U}_N(\phi_{m_n}^{\text{az}}, \phi_{m_n}^{\text{el}})$  can be

approximated as

$$\mathbf{U}_N(\phi_{m_n}^{\text{az}}, \phi_{m_n}^{\text{el}}) \approx [\mathbf{b}_N(\theta_{m_n}^{\text{el}}, \rho_n) \otimes \mathbf{a}_N(\theta_{m_n}^{\text{az}}, \rho_n)]^T \quad (21)$$

where

$$\mathbf{a}_N(\theta, \rho) = \left[ 1, e^{j2\pi \frac{d \cdot \theta}{d - \delta^T}}, \dots, e^{j2\pi \frac{d \cdot (P_h - 1) \theta}{d - (P_h - 1) \delta^T}} \right]^T \quad (22)$$

$$\mathbf{b}_N(\theta, \rho) = \left[ 1, e^{j2\pi \frac{-\delta^T + d \cdot \theta}{d - \delta^T}}, \dots, e^{j2\pi \frac{-(P_v - 1) \delta^T + d \cdot \theta}{d - (P_v - 1) \delta^T}} \right]^T \quad (23)$$

with  $d = 2[(P_h \delta^T)^2 + (P_v \delta^T)^2] \cdot \rho / \lambda$ .  $\mathbf{a}_N(\theta, \rho)$  and  $\mathbf{b}_N(\theta, \rho)$  are the horizontal and vertical steering vectors for near-field clusters, respectively.

For NPV clusters, the steering vector  $\hat{\mathbf{U}}_N(\phi_{m_n}^{\text{az}}, \phi_{m_n}^{\text{el}})$  is modified by ray visibility matrix  $\xi_{m_n}$  that consists of  $\xi_{pq, nm}$ .  $\hat{\mathbf{U}}_N(\phi_{m_n}^{\text{az}}, \phi_{m_n}^{\text{el}})$  can be written as

$$\hat{\mathbf{U}}_N(\phi_{m_n}^{\text{az}}, \phi_{m_n}^{\text{el}}) = \mathbf{U}_N(\phi_{m_n}^{\text{az}}, \phi_{m_n}^{\text{el}}) \odot \xi_{m_n}. \quad (24)$$

Furthermore, for NPV clusters, when  $\rho_n > 0.1$  is satisfied,  $\hat{\mathbf{U}}_N$  can be approximated as

$$\hat{\mathbf{U}}_N(\phi_{m_n}^{\text{az}}, \phi_{m_n}^{\text{el}}) \approx [\hat{\mathbf{b}}_N(\theta_{m_n}^{\text{el}}, \rho_n) \otimes \hat{\mathbf{a}}_N(\theta_{m_n}^{\text{az}}, \rho_n)]^T \quad (25)$$

where

$$\hat{\mathbf{a}}_N(\theta, \rho) = \left[ \mathbf{O}_{I_{s,n}^h - 1}, e^{j2\pi \frac{d \cdot (I_{e,n}^h - 1) \theta}{d - (I_{e,n}^h - 1) \delta^T}}, \dots, e^{j2\pi \frac{d \cdot (I_{e,n}^h - 1) \theta}{d - (I_{e,n}^h - 1) \delta^T}}, \mathbf{O}_{P_h - I_{e,n}^h} \right]^T \quad (26)$$

$$\hat{\mathbf{b}}_N(\theta, \rho) = \left[ \mathbf{O}_{I_{s,n}^v - 1}, e^{j2\pi \frac{-(I_{s,n}^v - 1) \delta^T + d \cdot \theta}{d - (I_{s,n}^v - 1) \delta^T}}, \dots, e^{j2\pi \frac{-(I_{e,n}^v - 1) \delta^T + d \cdot \theta}{d - (I_{e,n}^v - 1) \delta^T}}, \mathbf{O}_{P_v - I_{e,n}^v} \right]^T \quad (27)$$

with  $\mathbf{O}_n$  standing for a row vector with  $n$  zeros entries. Symbols  $I_{s,n}^{h/v}$  and  $I_{e,n}^{h/v}$  stand for the start and end column/row indices of the antenna elements in the cluster VR, respectively.

In this GBSM, for each cluster, all rays in the cluster share the same VR parameters. This means that the VR of ray in the cluster is no longer modeled separately. The VRs in the array domain is modeled in two stages. First, the independent length and position of the cluster VR in the horizontal and vertical directions are generated. Then, the VR length and position considering spatial consistency are calculated.

1) *Cluster VR Length*: The horizontal and vertical dimensions of the VR for the  $n$ th cluster  $\mathcal{L}_{C,n}^{h/v}$  is defined as

$$\mathcal{L}_{C,n}^{h/v} = (I_{e,n}^{h/v} - I_{s,n}^{h/v}) \cdot d_{h/v}. \quad (28)$$

In general, the VR lengths between different clusters and different directions are independent of each other and can be modeled as exponential distribution, i.e.,  $\mathcal{L}_{C,n}^{h/v} \sim \text{Exp}(\lambda_C^{h/v})$ , where  $\lambda_C^{h/v}$  is the rate parameter of the exponential distribution.

2) *Spatially Consistent Cluster VR Positions*: Spatially consistence means that two closely located clusters should have similar VRs positions. The concept of cluster distance is introduced to measure the distance between two clusters [52]. The distance between clusters  $n_1$  and  $n_2$  is calculated as

$$\text{CD}_{n_1 n_2} = \sqrt{\|\text{CD}_{\phi, n_1 n_2}\|^2 + \|\text{CD}_{\varphi, n_1 n_2}\|^2 + \text{CD}_{\tau, n_1 n_2}^2} \quad (29)$$

where

$$\text{CD}_{\phi/\varphi, n_1 n_2} = \frac{1}{2} \left| \Omega_{n_1}^{T/R} - \Omega_{n_2}^{T/R} \right| \quad (30)$$

and  $\Omega_n^{T/R}$  is angle unit vector of departure/arrival ray of the  $n$ th cluster ( $n = n_1, n_2$ ), i.e.,

$$\Omega_n^T = [\cos \phi_n^{\text{el}} \cos \phi_n^{\text{az}}, \cos \phi_n^{\text{el}} \sin \phi_n^{\text{az}}, \sin \phi_n^{\text{el}}]^T \quad (31)$$

$$\Omega_n^R = [\cos \varphi_n^{\text{el}} \cos \varphi_n^{\text{az}}, \cos \varphi_n^{\text{el}} \sin \varphi_n^{\text{az}}, \sin \varphi_n^{\text{el}}]^T \quad (32)$$

where  $\phi_n^{\text{el}}$ ,  $\phi_n^{\text{az}}$ ,  $\varphi_n^{\text{el}}$ , and  $\varphi_n^{\text{az}}$  are the mean values of elevation angle of departure (EAoD), azimuth angle of departure (AAoD), elevation angle of arrival (EAoA), and azimuth angle of arrival (AAoA) of the  $n$ th cluster, respectively. The delay distance can be written as

$$\text{CD}_{\tau, n_1 n_2} = \frac{|\tau_{n_1} - \tau_{n_2}|}{\Delta\tau_{\max}} \cdot \frac{\tau_{\text{std}}}{\Delta\tau_{\max}} \quad (33)$$

where  $\tau_n$  denotes the delay of the  $n$ th cluster,  $\Delta\tau_{\max} = \max(\tau_n) - \min(\tau_n)$ ,  $\tau_{\text{std}}$  is the standard deviation of cluster delays. Based on  $\text{CD}_{\tau, n_1 n_2}$ , spatially consistent VR positions can be generated using the exponential spatial filter method as follows [53]

$$\tilde{I}_{s, n_2}^{h/v} = \sum_{n_2 \in \mathcal{B}_{\text{NPV}}} \hat{I}_{s, n_1}^{h/v} \cdot \rho(n_1, n_2) \quad (34)$$

where  $\rho(n_1, n_2) = e^{-\frac{\text{CD}_{\tau, n_1 n_2}}{\Delta C}}$  is the exponential spatial filter and  $\Delta C$  is cluster correlation factor controlling the shape of the filter.  $\tilde{I}_{s, n_2}^{h/v} = [\tilde{I}_{s, k}^{h/v}]$  and  $\hat{I}_{s, n_1}^{h/v}$  are correlated and independent start column/row indices of antennas, respectively.

### III. BDCM FOR MASSIVE MIMO SYSTEMS

For environments where scatterers are not so abundant, BDCM exhibits obvious sparsity, which can be very helpful to reduce the complexity of system analysis. The BDCM is generated from the proposed GBSM by using a discrete Fourier transform (DFT)-based beamforming operation as follows

$$\mathbf{H}_B(t, f) = \tilde{\mathbf{V}}^H \mathbf{H}(t, f) \tilde{\mathbf{U}}^* \quad (35)$$

where  $\tilde{\mathbf{U}}$  and  $\tilde{\mathbf{V}}$  are transmitted beamforming matrices at Tx and Rx side, respectively. The operations  $(\cdot)^H$  and  $(\cdot)^*$  stand for conjugate-transpose and conjugate of the matrix, respectively. For Tx side,  $\tilde{\mathbf{U}}$  is defined as

$$\tilde{\mathbf{U}} = \tilde{\mathbf{U}}^{\text{el}} \otimes \tilde{\mathbf{U}}^{\text{az}} \quad (36)$$

$$\tilde{\mathbf{U}}^{\text{az}} = \frac{1}{\sqrt{P_h}} \left[ \mathbf{a} \left( \tilde{\theta}_{p_v}^{\text{az}} \right) \right]_{p_h=1, \dots, P_h} \in \mathbb{C}^{P_h \times P_h} \quad (37)$$

$$\tilde{\mathbf{U}}^{\text{el}} = \frac{1}{\sqrt{P_v}} \left[ \mathbf{b} \left( \tilde{\theta}_{p_v}^{\text{el}} \right) \right]_{p_v=1, \dots, P_v} \in \mathbb{C}^{P_v \times P_v} \quad (38)$$

where the columns of  $\tilde{\mathbf{U}}^{\text{az}}$  and  $\tilde{\mathbf{U}}^{\text{el}}$  are steering vectors associated with  $P_h$  and  $P_v$  uniformly spaced spatial frequencies with  $\tilde{\theta}_{p_h}^{\text{az}} = \frac{2p_h-1}{2P_h} - 0.5$  and  $\tilde{\theta}_{p_v}^{\text{el}} = \frac{2p_v-1}{2P_v} - 0.5$ . At Rx side, the transmit matrix  $\tilde{\mathbf{V}}$  is calculated as

$$\tilde{\mathbf{V}} = \tilde{\mathbf{V}}^{\text{el}} \otimes \tilde{\mathbf{V}}^{\text{az}} \quad (39)$$

where

$$\tilde{\mathbf{V}}^{\text{az}} = \frac{1}{\sqrt{Q_h}} \left[ \mathbf{a} \left( \tilde{\vartheta}_{q_h}^{\text{az}} \right) \right]_{q_h=1, \dots, Q_h} \in \mathbb{C}^{Q_h \times Q_h} \quad (40)$$

$$\tilde{\mathbf{V}}^{\text{el}} = \frac{1}{\sqrt{Q_v}} \left[ \mathbf{b} \left( \tilde{\vartheta}_{q_v}^{\text{el}} \right) \right]_{q_v=1, \dots, Q_v} \in \mathbb{C}^{Q_v \times Q_v} \quad (41)$$

The columns of  $\tilde{\mathbf{V}}^{\text{az}}$  and  $\tilde{\mathbf{V}}^{\text{el}}$  are steering vectors associated with  $Q_h$  and  $Q_v$  uniformly spaced spatial frequencies with  $\tilde{\vartheta}_{q_h}^{\text{az}} = \frac{2q_h-1}{2Q_h} - 0.5$  and  $\tilde{\vartheta}_{q_v}^{\text{el}} = \frac{2q_v-1}{2Q_v} - 0.5$ .

The BDCM in (35) can be calculated as

$$\begin{aligned} \mathbf{H}_B(t, f) &= \tilde{\mathbf{V}}^H \mathbf{H}(t, f) \tilde{\mathbf{U}}^* \\ &= \tilde{\mathbf{V}}^H [\mathbf{H}^{\text{FWV}}(t, f) + \mathbf{H}^{\text{NWV}}(t, f) + \mathbf{H}^{\text{NPV}}(t, f)] \tilde{\mathbf{U}}^* \\ &= \tilde{\mathbf{V}}^H \mathbf{H}^{\text{FWV}}(t, f) \tilde{\mathbf{U}}^* + \tilde{\mathbf{V}}^H \mathbf{H}^{\text{NWV}}(t, f) \tilde{\mathbf{U}}^* \\ &\quad + \tilde{\mathbf{V}}^H \mathbf{H}^{\text{FPV}}(t, f) \tilde{\mathbf{U}}^* \\ &= \mathbf{H}_B^{\text{FWV}}(t, f) + \mathbf{H}_B^{\text{NWV}}(t, f) + \mathbf{H}_B^{\text{NPV}}(t, f) \end{aligned} \quad (42)$$

where  $\mathbf{H}_B^{\text{FWV}}$ ,  $\mathbf{H}_B^{\text{NWV}}(t, f)$ , and  $\mathbf{H}_B^{\text{NPV}}(t, f)$  are the FWV, NWV, and NPV components of BDCM, respectively. The elements in  $\mathbf{H}_B(t, f)$  are written as  $\mathbf{H}_{B, \tilde{p}\tilde{q}}(t, f)$ , where  $\tilde{p}$  and  $\tilde{q}$  are the beam indices for Tx and Rx sides, respectively. The beam sampling is performed in both horizontal and vertical planes at the Tx side. The horizontal and vertical beams in the beam domain are similar to the azimuth and elevation angle in the spatial domain, respectively. The  $\tilde{p}$ th beam corresponds to the  $p_h$ th AAoD and  $p_v$ th EAoD. Similarly, at the Rx side, the  $\tilde{q}$ th beam corresponds to the  $q_h$ th EAoA and  $q_l$ th EAoA beam. The BDCM element  $\mathbf{H}_{B, \tilde{p}\tilde{q}}(t, f)$  can also be written as  $\mathbf{H}_{B, p_v p_h, q_v q_h}(t, f)$  and is expressed as

$$\begin{aligned} h_{B, p_v p_h, q_v q_h}(t, f) &= h_{B, p_v p_h, q_v q_h}^{\text{FWV}}(t, f) \\ &\quad + h_{B, p_v p_h, q_v q_h}^{\text{NWV}}(t, f) + h_{B, p_v p_h, q_v q_h}^{\text{NPV}}(t, f). \end{aligned} \quad (43)$$

By substituting the Channel matrix of the GBSM into (42) and (43), the elements of different types of clusters are calculated as

$$\begin{aligned} h_{B, p_v p_h, q_v q_h}^{\text{FWV}}(t, f) &= \frac{1}{\sqrt{PQ}} \sum_{n \in \mathcal{B}_{\text{FWV}}} \sum_{m=1}^{M_n} \beta_{m_n} \cdot e^{j[2\pi(\nu_{m_n} t - f\tau_{m_n}) + \Phi_{m_n}]} \end{aligned}$$

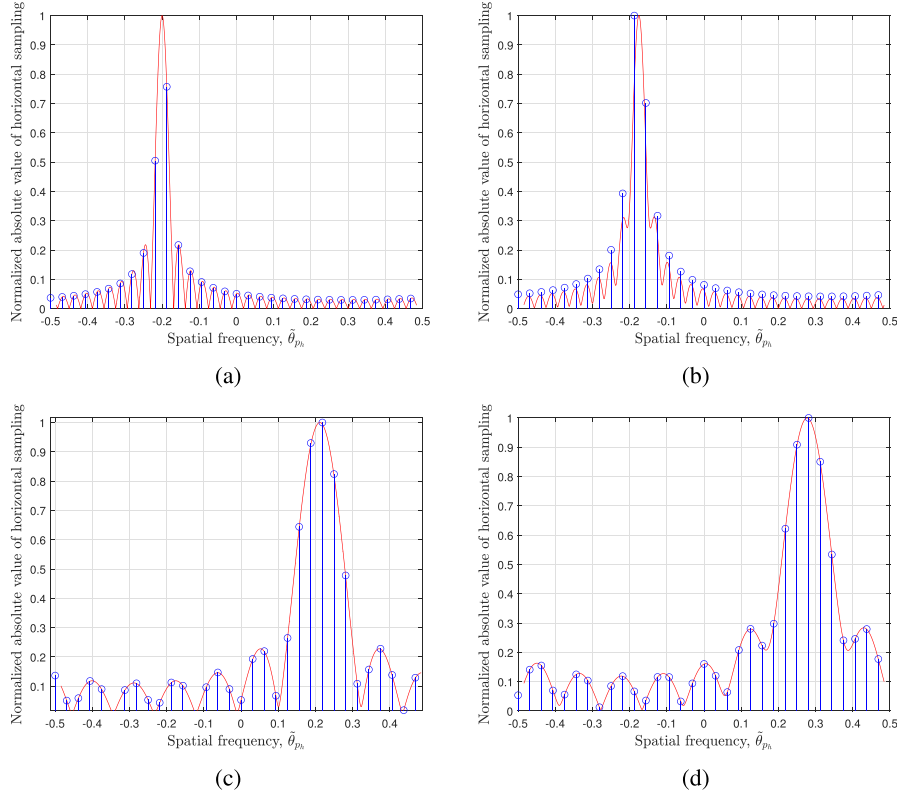


Fig. 3. Normalized absolute values of horizontal sampling of (a) NWV clusters ( $\rho = 0.8$ ), (b) NWV clusters ( $\rho = 0.5$ ), (c) NPV clusters ( $\rho = 0.5$ ,  $I_{\alpha,n}^v = 2$ ,  $I_{e,n}^v = 10$ ), and (d) NPV clusters ( $\rho = 0.08$ ,  $I_{\alpha,n}^v = 2$ ,  $I_{e,n}^v = 10$ ) ( $P_v = P_h = 32$ ).

$$\sum_{\alpha=0}^{Q_v-1} e^{j2\pi\alpha(\vartheta_{m_n}^{\text{el}} - \tilde{\vartheta}_{q_v}^{\text{el}})} \sum_{\beta=0}^{Q_h-1} e^{j2\pi\beta(\vartheta_{m_n}^{\text{az}} - \tilde{\vartheta}_{q_h}^{\text{az}})}$$

$$\sum_{a=0}^{P_v-1} e^{j2\pi a(\theta_{m_n}^{\text{el}} - \tilde{\theta}_{p_v}^{\text{el}})} \sum_{b=0}^{P_h-1} e^{j2\pi b(\theta_{m_n}^{\text{az}} - \tilde{\theta}_{p_h}^{\text{az}})} \quad (44)$$

$$h_{B,p_v p_h, q_v q_h}^{\text{NWV}}(t, f)$$

$$= \frac{1}{\sqrt{PQ}} \sum_{n \in \mathcal{B}_{\text{FWV}}} \sum_{m=1}^{M_n} \beta_{m_n} \cdot e^{j[2\pi(\nu_{m_n} t - f\tau_{m_n}) + \Phi_{m_n}]}$$

$$\sum_{\alpha=0}^{Q_v-1} e^{j2\pi\alpha(\vartheta_{m_n}^{\text{el}} - \tilde{\vartheta}_{q_v}^{\text{el}})} \sum_{\beta=0}^{Q_h-1} e^{j2\pi\beta(\vartheta_{m_n}^{\text{az}} - \tilde{\vartheta}_{q_h}^{\text{az}})}$$

$$\sum_{a=0}^{P_v-1} e^{j2\pi a \left( \frac{(a \cdot \delta^T + d \cdot \theta_{m_n}^{\text{el}}) \cdot a}{d - a \cdot \delta^T} - a \cdot \tilde{\theta}_{p_v}^{\text{el}} \right)} \sum_{b=0}^{P_h-1} e^{j2\pi b \left( \frac{d \cdot b \cdot \theta_{m_n}^{\text{az}}}{d - b \cdot \delta^T} - b \cdot \tilde{\theta}_{p_h}^{\text{az}} \right)}$$

$$(45)$$

$$h_{B,p_v p_h, q_v q_h}^{\text{NPV}}(t, f)$$

$$= \frac{1}{\sqrt{PQ}} \sum_{n \in \mathcal{B}_{\text{FWV}}} \sum_{m=1}^{M_n} \beta_{m_n} \cdot e^{j[2\pi(\nu_{m_n} t - f\tau_{m_n}) + \Phi_{m_n}]}$$

$$\sum_{\alpha=0}^{Q_v-1} e^{j2\pi\alpha(\vartheta_{m_n}^{\text{el}} - \tilde{\vartheta}_{q_v}^{\text{el}})} \sum_{\beta=0}^{Q_h-1} e^{j2\pi\beta(\vartheta_{m_n}^{\text{az}} - \tilde{\vartheta}_{q_h}^{\text{az}})}$$

$$\sum_{a=I_{s,n}^h-1}^{I_{e,n}^h-1} e^{j2\pi \left( \frac{(a \cdot \delta^T + d \cdot \theta_{m_n}^{\text{el}}) \cdot a}{d - a \cdot \delta^T} - a \cdot \tilde{\theta}_{p_v}^{\text{el}} \right)}$$

$$\times \sum_{b=I_{s,n}^v-1}^{I_{e,n}^v-1} e^{j2\pi \left( \frac{d \cdot b \cdot \theta_{m_n}^{\text{az}}}{d - b \cdot \delta^T} - b \cdot \tilde{\theta}_{p_h}^{\text{az}} \right)}. \quad (46)$$

From (44)–(46), one can observe that each formula consists of channel transmission parameters and sampling functions at both Tx and Rx sides. Each side contains horizontal and vertical sampling. The detailed derivations of (44)–(46) are shown in Appendix B.

Fig. 3 shows the normalized absolute values of horizontal sampling for NWV and NPV clusters in azimuth where  $P_h = P_v = 32$ . The NWV clusters can be observed by the whole 32 antennas and the VR of the NPV clusters cover 8 consecutive antennas. Fig. 3(a) and (b) present NPV clusters with different values of  $\rho$ . In the near-field case, the angles of departure of one cluster are quite different when impinging on different antenna elements. They may cover more than one beam. It can be seen that wholly visible clusters achieve their peak around  $\theta_{m_n}^{\text{el}}$ . For near-field clusters, the points of the peak value have an offset because the clusters are in several beams. Furthermore, the angle-width of the near-field cluster is much larger than that of the far-field cluster. This means that, when GBSM is transformed to beam domain, the near-field clusters will have multiple continuous nonzero elements. In addition, compared

with the FWV clusters, the angle-width for the PV cluster is wider due to the partial visibility. By comparing Fig. 3(c) and (d), one sees that, when the cluster is closer to the antenna, the angle-width is wider, which means that the cluster is located in more beams in the BDCM.

#### IV. CHANNEL STATISTICAL PROPERTIES OF THE PROPOSED GBSM AND BDCM

In this section, typical statistical properties of the proposed GBSM and BDCM are derived, including STF-CF, delay PSD, delay spread, Doppler PSD, and Doppler spread. In addition, beam spread and power leakage of the BDCM are calculated. Furthermore, the channel capacity of the channel with the channel transfer functions of these two channel models are derived.

##### A. STF-CF

The STF-CF of the proposed GBSM between  $h_{pq}(t, f)$  and  $h_{p'q'}(t + \Delta t, f + \Delta f)$  is calculated as

$$\begin{aligned} \Gamma_{pq,p'q'}(t, f, \Delta t, \Delta f) &= \mathbb{E} \{ h_{pq}^{\text{FWV}}(t, f) h_{p'q'}^{\text{FWV}*}(t + \Delta t, f + \Delta f) \} \\ &+ \mathbb{E} \{ h_{pq}^{\text{NWV}}(t, f) h_{p'q'}^{\text{NWV}*}(t + \Delta t, f + \Delta f) \} \\ &+ \mathbb{E} \{ h_{pq}^{\text{NPV}}(t, f) h_{p'q'}^{\text{NPV}*}(t + \Delta t, f + \Delta f) \} \quad (47) \end{aligned}$$

where  $\Delta t$  and  $\Delta f$  is the short period and frequency between two adjacent instants and frequency bands, respectively.

In order to facilitate the distinction, we use  $\Gamma$  to represent the STF-CF of the GBSM, while the STF-CF of the BDCM is denoted as  $\gamma$ . The STF-CF of the proposed BDCM between  $h_{B,p_v p_h, q_v q_h}(t, f)$  and  $h_{B,p'_v p'_h, q'_v q'_h}(t + \Delta t, f + \Delta f)$  is defined as

$$\begin{aligned} \gamma_{p_v p_h, q_v q_h, p'_v p'_h, q'_v q'_h}(t, f, \Delta t, \Delta f) &= \mathbb{E} \left\{ h_{B,p_v p_h, q_v q_h}(t, f) h_{B,p'_v p'_h, q'_v q'_h}^*(t + \Delta t, f + \Delta f) \right\}. \quad (48) \end{aligned}$$

The STF-CF can be further shown as a sum of FWV, NWV, and NPV components

$$\begin{aligned} \gamma_{p_v p_h, q_v q_h, p'_v p'_h, q'_v q'_h}(t, f, \Delta t, \Delta f) &= \gamma_{p_v p_h, q_v q_h, p'_v p'_h, q'_v q'_h}^{\text{FWV}}(t, f, \Delta t, \Delta f) \\ &+ \gamma_{p_v p_h, q_v q_h, p'_v p'_h, q'_v q'_h}^{\text{NWV}}(t, f, \Delta t, \Delta f) \\ &+ \gamma_{p_v p_h, q_v q_h, p'_v p'_h, q'_v q'_h}^{\text{NPV}}(t, f, \Delta t, \Delta f). \quad (49) \end{aligned}$$

By substituting (44)–(46) into (49), the FWV, NWV, and NPV components of STF-CF can be further expressed as

$$\begin{aligned} \gamma_{p_v p_h, q_v q_h, p'_v p'_h, q'_v q'_h}^{\text{FWV}}(t, f, \Delta t, \Delta f) &= \mathbb{E} \left\{ h_{B,p_v p_h, q_v q_h}^{\text{FWV}}(t, f) h_{B,p'_v p'_h, q'_v q'_h}^{\text{FWV}*}(t + \Delta t, f + \Delta f) \right\} \\ &= \mathbb{E} \left\{ \frac{1}{PQ} \sum_{n \in \mathcal{B}_{\text{FWV}}} \sum_{m=1}^{M_n} \beta_{m_n}^2 \cdot e^{j[2\pi(\Delta f \tau_{m_n} - \nu_{m_n} \Delta t)]} \right\} \end{aligned}$$

$$\begin{aligned} &\sum_{\alpha=0}^{Q_v-1} e^{j2\pi\alpha(\vartheta_{m_n}^{\text{el}} - \tilde{\vartheta}_{q'_v}^{\text{el}})} \sum_{\alpha=0}^{Q_v-1} e^{j2\pi\alpha(\vartheta_{m_n}^{\text{el}} - \tilde{\vartheta}_{q'_v}^{\text{el}})} \\ &\sum_{\beta=0}^{Q_h-1} e^{j2\pi\beta(\vartheta_{m_n}^{\text{az}} - \tilde{\vartheta}_{q'_h}^{\text{az}})} \sum_{\beta=0}^{Q_h-1} e^{j2\pi\beta(\vartheta_{m_n}^{\text{az}} - \tilde{\vartheta}_{q'_h}^{\text{az}})} \\ &\times \sum_{a=0}^{P_v-1} e^{j2\pi a(\theta_{m_n}^{\text{el}} - \tilde{\theta}_{p'_v}^{\text{el}})} \\ &\sum_{a=0}^{P_v-1} e^{j2\pi a(\theta_{m_n}^{\text{el}} - \tilde{\theta}_{p'_v}^{\text{el}})} \sum_{b=0}^{P_h-1} e^{j2\pi b(\theta_{m_n}^{\text{az}} - \tilde{\theta}_{p'_h}^{\text{az}})} \\ &\times \sum_{b=0}^{P_h-1} e^{j2\pi b(\theta_{m_n}^{\text{az}} - \tilde{\theta}_{p'_h}^{\text{az}})} \} \quad (50) \end{aligned}$$

$$\begin{aligned} \gamma_{p_v p_h, q_v q_h, p'_v p'_h, q'_v q'_h}^{\text{NWV}}(t, f, \Delta t, \Delta f) &= \mathbb{E} \left\{ h_{B,p_v p_h, q_v q_h}^{\text{NWV}}(t, f) h_{B,p'_v p'_h, q'_v q'_h}^{\text{NWV}*}(t + \Delta t, f + \Delta f) \right\} \\ &= \mathbb{E} \left\{ \frac{1}{PQ} \sum_{n \in \mathcal{B}_{\text{NWV}}} \sum_{m=1}^{M_n} \beta_{m_n}^2 \cdot e^{j[2\pi(\Delta f \tau_{m_n} - \nu_{m_n} \Delta t)]} \right. \\ &\sum_{\alpha=0}^{Q_v-1} e^{j2\pi\alpha(\vartheta_{m_n}^{\text{el}} - \tilde{\vartheta}_{q'_v}^{\text{el}})} \sum_{\alpha=0}^{Q_v-1} e^{j2\pi\alpha(\vartheta_{m_n}^{\text{el}} - \tilde{\vartheta}_{q'_v}^{\text{el}})} \\ &\sum_{\beta=0}^{Q_h-1} e^{j2\pi\beta(\vartheta_{m_n}^{\text{az}} - \tilde{\vartheta}_{q'_h}^{\text{az}})} \sum_{\beta=0}^{Q_h-1} e^{j2\pi\beta(\vartheta_{m_n}^{\text{az}} - \tilde{\vartheta}_{q'_h}^{\text{az}})} \\ &\sum_{a=0}^{P_v-1} e^{j2\pi \left( \frac{(a \cdot \delta^{\text{T}} + d \cdot \theta) \cdot a}{d - a \cdot \delta^{\text{T}}} - a \cdot \tilde{\theta}_{p'_v}^{\text{el}} \right)} \sum_{a=0}^{P_v-1} e^{j2\pi \left( \frac{(a \cdot \delta^{\text{T}} + d \cdot \theta) \cdot a}{d - a \cdot \delta^{\text{T}}} - a \cdot \tilde{\theta}_{p'_v}^{\text{el}} \right)} \\ &\left. \sum_{b=0}^{P_h-1} e^{j2\pi \left( \frac{d \cdot b \cdot \theta_{m_n}^{\text{az}}}{d - b \cdot \delta^{\text{T}}} - b \cdot \tilde{\theta}_{p'_h}^{\text{az}} \right)} \sum_{b=0}^{P_h-1} e^{j2\pi \left( \frac{d \cdot b \cdot \theta_{m_n}^{\text{az}}}{d - b \cdot \delta^{\text{T}}} - b \cdot \tilde{\theta}_{p'_h}^{\text{az}} \right)} \right\} \quad (51) \end{aligned}$$

$$\begin{aligned} \gamma_{p_v p_h, q_v q_h, p'_v p'_h, q'_v q'_h}^{\text{NPV}}(t, f, \Delta t, \Delta f) &= \mathbb{E} \left\{ h_{B,p_v p_h, q_v q_h}^{\text{NPV}}(t, f) h_{B,p'_v p'_h, q'_v q'_h}^{\text{NPV}*}(t + \Delta t, f + \Delta f) \right\} \\ &= \mathbb{E} \left\{ \frac{1}{PQ} \sum_{n \in \mathcal{B}_{\text{NPV}}} \sum_{m=1}^{M_n} \beta_{m_n}^2 \cdot e^{j[2\pi(\Delta f \tau_{m_n} - \nu_{m_n} \Delta t)]} \right. \\ &\sum_{\alpha=0}^{Q_v-1} e^{j2\pi\alpha(\vartheta_{m_n}^{\text{el}} - \tilde{\vartheta}_{q'_v}^{\text{el}})} \sum_{\alpha=0}^{Q_v-1} e^{j2\pi\alpha(\vartheta_{m_n}^{\text{el}} - \tilde{\vartheta}_{q'_v}^{\text{el}})} \\ &\sum_{\beta=0}^{Q_h-1} e^{j2\pi\beta(\vartheta_{m_n}^{\text{az}} - \tilde{\vartheta}_{q'_h}^{\text{az}})} \sum_{\beta=0}^{Q_h-1} e^{j2\pi\beta(\vartheta_{m_n}^{\text{az}} - \tilde{\vartheta}_{q'_h}^{\text{az}})} \\ &\sum_{a=I_{e,n}^h-1} e^{j2\pi \left( \frac{(a \cdot \delta^{\text{T}} + d \cdot \theta) \cdot a}{d - a \cdot \delta^{\text{T}}} - a \cdot \tilde{\theta}_{p'_v}^{\text{el}} \right)} \\ &\left. \sum_{a=I_{s,n}^h-1} e^{j2\pi \left( \frac{(a \cdot \delta^{\text{T}} + d \cdot \theta) \cdot a}{d - a \cdot \delta^{\text{T}}} - a \cdot \tilde{\theta}_{p'_v}^{\text{el}} \right)} \right\} \end{aligned}$$

$$\left. \begin{aligned} & \sum_{b=I_{s,n}^v-1}^{I_{s,n}^v-1} e^{j2\pi \left( \frac{d \cdot b \cdot \theta_{m,n}^{az}}{d-b \cdot \delta^1} - b \cdot \tilde{\theta}_{p_v}^{az} \right)} \\ & \sum_{b=I_{s,n}^v-1}^{I_{s,n}^v-1} e^{j2\pi \left( \frac{d \cdot b \cdot \theta_{m,n}^{az}}{d-b \cdot \delta^1} - b \cdot \tilde{\theta}_{p_h}^{az} \right)} \end{aligned} \right\} \quad (52)$$

### B. Delay PSD and Delay Spread

The delay PSD gives the distribution of signal power received over a multipath channel as a function of propagation delays. In the proposed BDCM, the delay PSD  $\psi(t, \tau)$  can be calculated by the Fourier transform of the frequency correlation function as

$$\psi(t, \tau) = \int_{-\infty}^{\infty} \gamma_{p_v p_h, q_v q_h}(t, f, \Delta f) e^{j2\pi \tau \Delta f} d\Delta f. \quad (53)$$

The delay spread  $\sigma_\tau$  of the channel is calculated by

$$\sigma_\tau = \sqrt{\frac{\int_0^\infty (\tau - \mu_\tau)^2 \psi(t, \tau) d\tau}{\int_0^\infty \psi(t, \tau) d\tau}} \quad (54)$$

where  $\mu_\tau = \frac{\int_0^\infty \tau \psi(t, \tau) d\tau}{\int_0^\infty \psi(t, \tau) d\tau}$  is the mean delay of the channel. The delay PSD of the proposed BDCM can be calculated by replacing  $\gamma_{p_v p_h, q_v q_h}(t, f, \Delta f)$  in (53) with  $\Gamma_{pq}(t, f, \Delta f)$ .

### C. Doppler PSD and Doppler Spread

The Doppler PSD gives the average power at the channel output as a function of the Doppler frequency. In the proposed BDCM, the Doppler PSD  $\psi_D(t, f, \nu)$  can be calculated by the Fourier transform of the temporal ACF as

$$\psi_D(t, f, \nu) = \int_{-\infty}^{\infty} \gamma_{p_v p_h, q_v q_h}(t, f, \Delta t) e^{j2\pi \nu \Delta t} d\Delta t. \quad (55)$$

The Doppler spread  $\sigma_\nu$  of the channel is calculated by

$$\sigma_\nu(t, f) = \sqrt{\frac{\int_0^\infty (\nu - \mu_\nu)^2 \psi_D(t, f, \nu) d\nu}{\int_0^\infty \psi_D(t, f, \nu) d\nu}} \quad (56)$$

where  $\mu_\nu = \frac{\int_0^\infty \nu \psi_D(t, f, \nu) d\nu}{\int_0^\infty \psi_D(t, f, \nu) d\nu}$  is the mean Doppler frequency of the BDCM.

### D. RMS Beam Spread

The beam spread describes the power dispersion of the beam domain channel over different beam directions. Similar to the RMS angular spread, the RMS azimuth beam spread can be defined as

$$\sigma_B^{az} = \sqrt{\frac{\sum_{p_v, p_h=1}^{P_h, P_v} |h_{B, p_v p_h}|^2 (\tilde{\phi}_{p_h}^{az} - \mu^{az})^2}{\sum_{p_v, p_h=1}^{P_h, P_v} |h_{B, p_v p_h}|^2}} \quad (57)$$

where  $\mu^{az} = \frac{\sum_{p_v, p_h=1}^{P_h, P_v} |h_{B, p_v p_h}| (\tilde{\phi}_{p_h}^{az} - \mu^{az})}{\sum_{p_v, p_h=1}^{P_h, P_v} |h_{B, p_v p_h}|^2}$  is the mean beam azimuth angle of the BDCM.

### E. Power Leakage

In the BDCM, the power of some rays will inevitably be spread over a series of beam directions, which is called power

leakage [54]. Power leakage is a major concern in massive MIMO communication systems. Power leakage in the beam domain may result in a significant degradation in the signal-to-noise ratio and the transmission rate [55]. The ratio of power leakage provides the motivation for linear precoder designs and channel estimation algorithms. In the traditional BDCM, the power leakage is caused by the mismatch between physical path angles and the spatial frequency sampling points [55]. However, existing researches have ignored the effects of near-field clusters and partly visible clusters, which reduces the accuracy of the channel model for evaluating massive MIMO systems. The power leakage for NWV and NPV clusters can be defined as

$$\Gamma^{\text{NWV}} = 1 - \frac{\sum_{p_h \in \mathcal{U}(\theta_{p_h}^{az}, K_h), p_v \in \mathcal{U}(\theta_{p_v}^{el}, K_v)} |h_{B, p_v p_h, q_v q_h}^{\text{NWV}}|^2}{\sum_{p_v, p_h=1}^{P_v, P_h} |h_{B, p_v p_h, q_v q_h}^{\text{NWV}}|^2} \quad (58)$$

$$\Gamma^{\text{NPV}} = 1 - \frac{\sum_{p_h \in \mathcal{U}(\theta_{p_h}^{az}, K_h), p_v \in \mathcal{U}(\theta_{p_v}^{el}, K_v)} |h_{B, p_v p_h, q_v q_h}^{\text{NPV}}|^2}{\sum_{p_v, p_h=1}^{P_v, P_h} |h_{B, p_v p_h, q_v q_h}^{\text{NPV}}|^2} \quad (59)$$

where  $\mathcal{U}(\theta_{p_h}^{az}, K_h)$  and  $\mathcal{U}(\theta_{p_v}^{el}, K_v)$  are column and row index sets for a  $K_h \times K_v$  sub-matrix centering around the physical direction of the cluster. Therefore, the power leakage in (58) and (59) is actually measured by calculating the ratio of the power of the  $K_h \times K_v$  sub-matrix around the main lobe direction to the total channel power.

### F. Channel Capacity

The channel capacity is defined to be the highest rate at which information can be sent with arbitrarily low error. When Rx knows the perfect channel state information (CSI) and the Tx does not have CSI, the ergodic channel capacity of the proposed BDCM can be calculated as

$$C = \mathbb{E} \left\{ \log_2 \det \left( \mathbf{I} + \frac{\rho_{\text{SNR}}}{P} \bar{\mathbf{H}} \bar{\mathbf{H}}^H \right) \right\} \quad (60)$$

where  $\rho_{\text{SNR}}$  is the signal-to-noise ratio (SNR) and  $P$  is the total number of Tx array,  $\bar{\mathbf{H}}$  is the normalized channel matrix, which can be obtained by

$$\bar{\mathbf{H}} = \mathbf{H} \cdot \left\{ \frac{1}{PQ} \|\mathbf{H}\|_F \right\}^{-\frac{1}{2}} \quad (61)$$

where  $\mathbf{H}$  is the channel transfer matrix and  $\|\cdot\|_F$  calculates the Frobenius norm of a matrix. The analytical expressions of channel capacities of the GBSM and BDCM can be obtained by substituting  $\mathbf{H}(t, f)$  in (11) and  $\mathbf{H}_B(t, f)$  in (35) into (60), respectively. Considering the large bandwidth at the THz band, frequency-dependent parameters are generated by evolution in the frequency domain, which is introduced in [38]. Therefore, the channel capacity is frequency-dependent. The GBSM and the BDCM reflect the same physical environment in the spatial and beam domain, respectively. Thus, they have the same theoretical channel capacity.

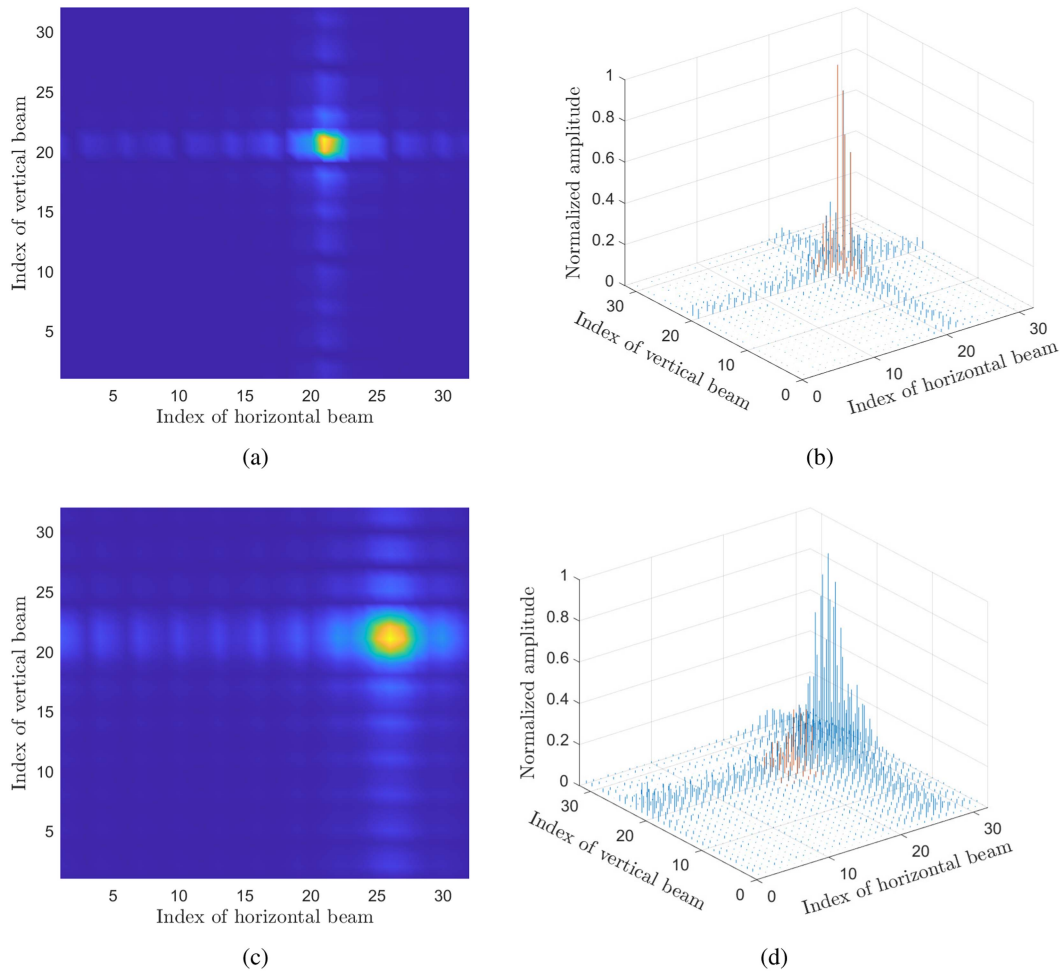


Fig. 4. Illustrations of the beam pattern for a single NPV cluster (a) beam pattern ( $\rho = 0.5$ ,  $I_{s,n}^v = 1$ ,  $I_{e,n}^v = 20$ ), (b) normalized amplitude distribution ( $\rho = 0.5$ ,  $I_{s,n}^v = 1$ ,  $I_{e,n}^v = 20$ ), (c) beam pattern ( $\rho = 0.1$ ,  $I_{s,n}^v = 10$ ,  $I_{e,n}^v = 20$ ), and (d) normalized amplitude distribution ( $\rho = 0.1$ ,  $I_{s,n}^v = 10$ ,  $I_{e,n}^v = 20$ ).

## V. RESULTS AND ANALYSIS

In this section, to validate the performance of proposed THz BDCM, the statistical properties of the THz BDCM are simulated and discussed. The frequency of the system is chosen at 300 GHz. Both  $\delta_T$  and  $\delta_R$  equal to half of the wavelength at 300 GHz. Basic simulation parameters for a typical THz indoor scenario are set as follows. Considering the high reflection loss [22], the total number of clusters is assumed as 10, which consists of 2 FWV clusters, 2 NWV clusters, and 6 NPV clusters. The parameters for the GBSM are generated in [38], including the delay, phase, and power of each ray. We can generate the complete CIR of the proposed GBSM and BDCM using these channel parameters and antenna configuration. Then, the statistical properties are simulated by using equations derived in Section IV. The velocity of Rx is  $v^R = 0.6$  m/s in the horizontal plane and the moving direction is  $\frac{\pi}{3}$ . The velocity of Tx is  $v^T = 0$  m/s.

In order to understand the significance of power leakage more intuitively, the beam pattern and normalized amplitude distribution of a single NPV cluster are presented in Fig. 4. One cluster mainly focus at one horizontal and vertical beam, which

proves the sparsity of BDCM. The sparsity of the BDCM is helpful in reducing the overhead of signal estimation complexity at transceivers [45], [46]. The power leakage in the same horizontal or vertical angle can also be observed. By comparing Fig. 4(a) and (c), we can see that the  $\rho$  and the VR length have great influences on the beam pattern. In Fig. 4(b) and (d), the amplitudes of  $6 \times 6$  channel elements around the direction are indicated by red lines. It can be seen that when the scatterer is closer to the antenna, the spherical wavefront leads to obvious power leakage. The center of the pattern have a great offset of the specific AAoD. This is because when the cluster is close to antenna array, the angles of departure for all elements are not consistent. In view of the whole antenna array, the angle has a range. As a result, the cluster can be observed by more beams. In practice, the offset and power leakage of near-field scatterers will need to be considered.

In order to better evaluate the influence of different parameters on power leakage, we compare the power leakage with increased VR length under different antenna configurations and different scatterers distances in Fig. 5. From Fig. 5(a), one sees that for the same antenna configuration, when the VR length increases, the power leakage decreases. When the VR length is larger than

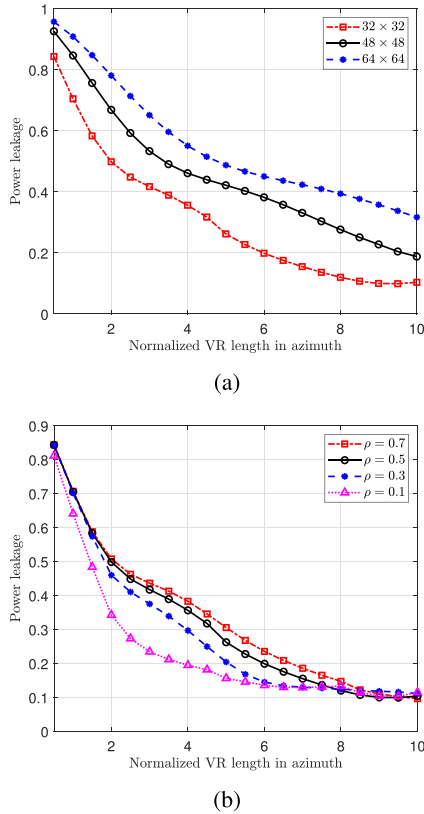


Fig. 5. Illustrations of the power leakage with different normalized VR length in azimuth (a) for different  $P_v \times P_h$  ( $\rho = 0.5$ ,  $\phi_{m_n}^{az} = \pi/4$ ,  $\phi_{m_n}^{el} = \pi/4$ ) and (b) for different  $\rho$  ( $P_v = P_h = 32$ ).

6 elements, the power leakage is reduced slowly. For larger antenna arrays, the power leakage is higher under the same VR length, because the visible region accounts for a smaller proportion of the whole antenna. In Fig. 5(b), different scatterers distances are compared, the closer scatterer from the antenna leads to more power leakage.

In order to better evaluate the influence of spherical wavefront on STF-CF, we simulate the channels with spherical wavefront in the case of FWV clusters is ignored. When we simulate the channels with planar wavefront, only FWV is considered. The ACFs of the GBSM and BDCM are compared in Fig. 6. one sees that the ACFs of the GBSM and BDCM match well, which means that the transmission in spatial domain has no influence on time correlation. In addition, we compare the ACFs with planar wavefront and spherical wavefront, we can see the small differences between these two clusters. The correlation of the scatterers in near-field positions is smaller compared with the scatterers in far-field areas. This is because the Doppler effect of closer cluster has larger impact than that of far-field clusters. To validate the performance of the proposed THz BDCM, the FCFs of the GBSM and BDCM are simulated in Fig. 7, the FCFs of the GBSM and BDCM match well. The beam transmission in spatial domain has no influence on frequency correlation either. In addition, we also compare the FCFs of channels with planar and spherical wavefront. We can see the obvious differences between these two types of clusters. The frequency correlation

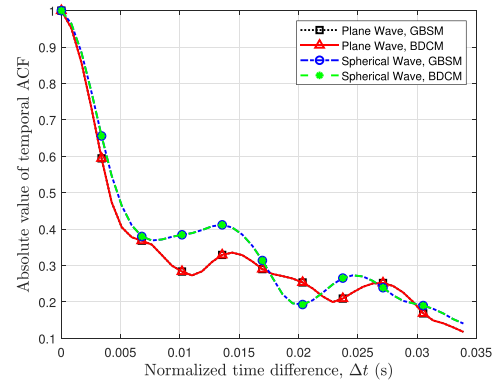


Fig. 6. Temporal ACFs of GBSM and BDCM for different clusters ( $P_v = P_h = 32$ ,  $Q_v = Q_h = 4$ ,  $f_c = 300$  GHz,  $v^R = 0.6$  m/s,  $v^T = 0$ ,  $\rho = 0.5$ ,  $I_{s,n}^v = 1$ ,  $I_{e,n}^v = 20$ ).

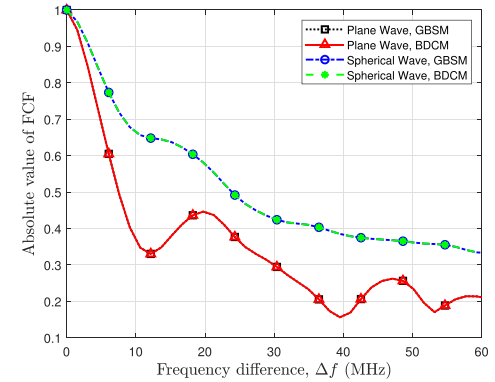


Fig. 7. FCFs of GBSM and BDCM for different clusters ( $P_v = P_h = 32$ ,  $Q_v = Q_h = 4$ ,  $f_c = 300$  GHz,  $v^R = 0.6$  m/s,  $v^T = 0$ ,  $\rho = 0.5$ ,  $I_{s,n}^v = 1$ ,  $I_{e,n}^v = 20$ ).

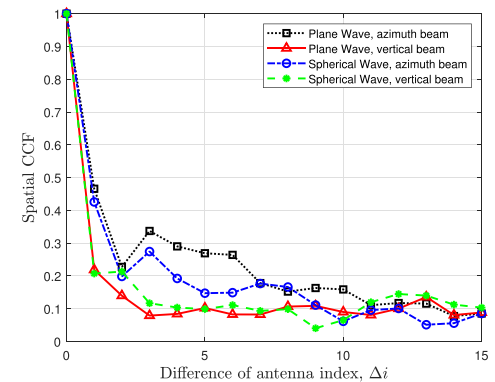


Fig. 8. SCCFs of the BDCM for different clusters ( $P_v = P_h = 32$ ,  $Q_v = Q_h = 4$ ,  $f_c = 300$  GHz,  $v^R = 0.6$  m/s,  $v^T = 0$ ,  $\rho = 0.5$ ,  $I_{s,n}^v = 1$ ,  $I_{e,n}^v = 20$ ).

of scatterers in near-field regions is higher than that of clusters in far-field regions.

In Fig. 8, we compare the spatial CCFs of the proposed BDCM. Here, both horizontal and vertical planes are simulated with plane or spherical wave. The correlation of different planes is different because the angular deviation caused by spherical wavefront is different in horizontal and vertical planes. From Figs. 6–8, one can obviously observe the influence of spherical

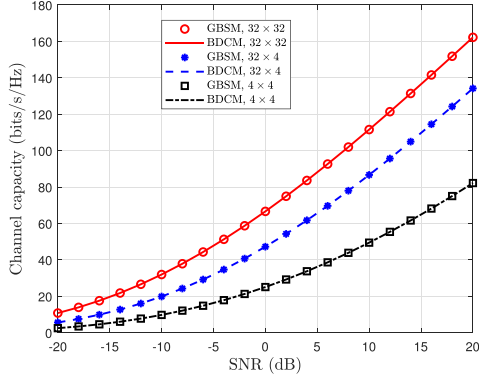


Fig. 9. Channel capacities of GBSM and BDCM with different Tx antenna configurations ( $Q_v = Q_h = 4$ ,  $f_c = 300$  GHz,  $v^R = 0.6$  m/s,  $v^T = 0$ ,  $\rho = 0.5$ ,  $I_{s,n}^v = 1$ ,  $I_{e,n}^v = 20$ ).

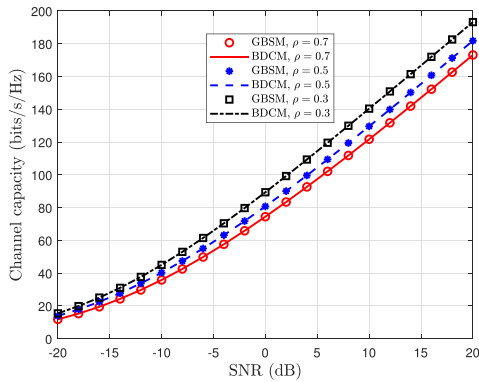


Fig. 10. Channel capacities of GBSM and BDCM with different  $\rho$  ( $P_v = P_h = 32$ ,  $Q_v = Q_h = 4$ ,  $f_c = 300$  GHz,  $v^R = 0.6$  m/s,  $v^T = 0$ ,  $I_{s,n}^v = 1$ ,  $I_{e,n}^v = 20$ ).

wavefront on correlation functions in space, time, and frequency domains, which shows that the spherical effect cannot be neglected for an accurate channel model.

Fig. 9 compares channel capacities of different Tx antenna configurations with SNR from -20 dB to 20 dB. For massive MIMO, we can see that the GBSM and BDCM have the same channel capacities, which proves that the proposed BDCM can be used in system performance analysis. In Fig. 10, we investigate the channel capacities with different near-field clusters. When the scatterers are in the closer positions, the channel capacity becomes larger.

## VI. CONCLUSION

In this paper, a novel 3D THz GBSM and the corresponding BDCM have been proposed for 6G THz massive MIMO wireless communication systems. The propagation mechanisms of the THz band, such as non-negligible diffuse scattering and limited order of reflection, have been contained. The characteristics of massive MIMO have also been considered, including the spherical wavefront and spatial non-stationarity. We have divided all the clusters into three types and derived the corresponding steering vectors. Moreover, we have simplified the steering vectors of the GBSM and transformed the GBSM to the BDCM by

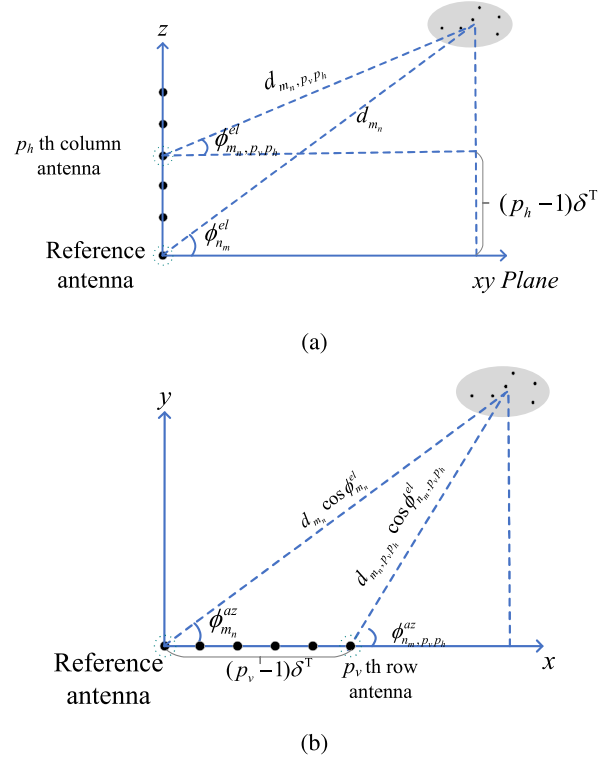


Fig. 11. Schematic diagram of geometric relationship in (a) vertical plane and (b) horizontal plane.

using a Fourier transform matrix in both horizontal and vertical directions. Statistical properties of the proposed THz GBSM and BDCM have been derived and investigated. By simulations and comparisons between STF-CFs and channel capacities of the GBSM and BDCM, we have found that the statistical properties of the proposed BDCM match well with those of the GBSM. The proposed GBSM and BDCM can obviously reflect the influence of the spherical wavefront and VRs on channel statistical properties. Spherical wavefront has been proved to result in higher temporal and frequency correlations than planar wavefront. In addition, clusters in nearer regions contribute to a small increase of the channel capacity. Furthermore, the BDCM exhibits significant sparsity, which is very helpful in reducing the complexity of the GBSM and improve the mathematical tractability of THz system design, performance evaluation, and optimization.

## APPENDIX A DERIVATIONS OF (9) AND (10)

To calculate steering vector for near-field clusters, we need to select one antenna as reference antenna to calculate the distances and angles of all other antennas. Without loss of generality, we take the element in the first row and the first column as the reference antenna. The geometric relationship of  $[d_{m_n}, \phi_{m_n}^{el}, \phi_{m_n}^{az}]$  and  $[d_{m_n, p_v, p_h}, \phi_{m_n, p_v, p_h}^{el}, \phi_{m_n, p_v, p_h}^{az}]$  is shown in Fig. 11. By comparing the distance difference between  $d_{m_n}$  and  $d_{m_n, p_v, p_h}$  in horizontal plane and the vertical plane,  $[d_{m_n, p_v, p_h}, \phi_{m_n, p_v, p_h}^{el}, \phi_{m_n, p_v, p_h}^{az}]$  of all antenna elements can be

calculated by  $[d_{m_n}, \phi_{m_n}^{\text{el}}, \phi_{m_n}^{\text{az}}]$  as

$$d_{m_n} \cos \phi_{m_n}^{\text{el}} \cos \phi_{m_n}^{\text{az}} - d_{m_n, p_v p_h} \cos \phi_{m_n, p_v p_h}^{\text{el}} \cos \phi_{m_n, p_v p_h}^{\text{az}} = (p_v - 1) \delta^T \quad (62)$$

$$d_{m_n} \sin \phi_{m_n}^{\text{el}} - d_{m_n, p_v p_h} \sin \phi_{m_n, p_v p_h}^{\text{el}} = (p_h - 1) \delta^T \quad (63)$$

$$d_{m_n} \cos \phi_{m_n}^{\text{el}} \sin \phi_{m_n}^{\text{az}} = d_{m_n, p_v p_h} \cos \phi_{m_n, p_v p_h}^{\text{el}} \sin \phi_{m_n, p_v p_h}^{\text{az}}. \quad (64)$$

By simultaneous three equations (62)–(64), we get the solution of  $d_{m_n, p_v p_h}$ ,  $\phi_{m_n, p_v p_h}^{\text{el}}$ , and  $\phi_{m_n, p_v p_h}^{\text{az}}$  as

$$\begin{cases} d_{m_n, p_v p_h} \\ \phi_{m_n, p_v p_h}^{\text{el}} \\ \phi_{m_n, p_v p_h}^{\text{az}} \end{cases} = \begin{cases} \sqrt{a^2 + b^2 + d_{m_n}^2 - 2bd_{m_n} \cos \phi_{m_n}^{\text{el}} \cos \phi_{m_n}^{\text{az}} - 2ad_{m_n} \sin \phi_{m_n}^{\text{el}}} \\ \arctan \left[ \frac{-a + d_{m_n} \sin \cos \phi_{m_n}^{\text{el}}}{\sqrt{b^2 + d_{m_n}^2 \cos^2 \phi_{m_n}^{\text{el}} - 2bd_{m_n} \cos \phi_{m_n}^{\text{el}} \cos \phi_{m_n}^{\text{az}}}} \right] \\ \arctan \left[ \frac{d_{m_n} \cos \phi_{m_n}^{\text{el}} \sin \phi_{m_n}^{\text{az}}}{b - d_{m_n} \cos \phi_{m_n}^{\text{el}} \cos \phi_{m_n}^{\text{az}}} \right] \end{cases} \quad (65)$$

where  $a = (p_h - 1) \delta^T$  and  $b = (p_v - 1) \delta^T$ . Then, the expressions of  $\cos \phi_{m_n, p_v p_h}^{\text{el}}$ ,  $\sin \phi_{m_n, p_v p_h}^{\text{az}}$  and  $\sin \phi_{m_n, p_v p_h}^{\text{el}}$  can be obtained in (9) and (10), respectively.

## APPENDIX B

### DERIVATIONS OF (44)–(46)

The CTF of BDCM  $\mathbf{H}_B(t, f)$  is calculated by the Fourier transformation from the CTF of GBSM  $\mathbf{H}(t, f)$  as

$$\begin{aligned} \mathbf{H}_B(t, f) &= \tilde{\mathbf{V}}^H \mathbf{H}(t, f) \tilde{\mathbf{U}}^* \\ &= [\tilde{\mathbf{V}}^{\text{el}} \otimes \tilde{\mathbf{V}}^{\text{az}}]^H \mathbf{H}(t, f) [\tilde{\mathbf{U}}^{\text{el}} \otimes \tilde{\mathbf{U}}^{\text{az}}]^* \\ &= [\tilde{\mathbf{V}}^{\text{el}} \otimes \tilde{\mathbf{V}}^{\text{az}}]^H (\mathbf{H}^{\text{FWV}}(t, f) + \mathbf{H}^{\text{NWV}}(t, f) \\ &\quad + \mathbf{H}^{\text{NPV}}(t, f)) [\tilde{\mathbf{U}}^{\text{el}} \otimes \tilde{\mathbf{U}}^{\text{az}}]^*. \end{aligned} \quad (66)$$

By substituting (12), (13), and (14) into (66), the transmission matrix of three kinds of clusters can be calculated as

$$\begin{aligned} \mathbf{H}_B^{\text{FWV}}(t, f) &= [\tilde{\mathbf{V}}^{\text{el}} \otimes \tilde{\mathbf{V}}^{\text{az}}]^H \mathbf{H}^{\text{FWV}}(t, f) [\tilde{\mathbf{U}}^{\text{el}} \otimes \tilde{\mathbf{U}}^{\text{az}}]^* \\ &= [\tilde{\mathbf{V}}^{\text{el}} \otimes \tilde{\mathbf{V}}^{\text{az}}]^H \left[ \sum_{n \in \mathcal{B}_{\text{FWV}}} \sum_{m=1}^{M_n} \beta_{m_n} \cdot e^{j[2\pi(\nu_{m_n} t - f \tau_{m_n}) + \Phi_{m_n}]} \right. \\ &\quad \left. \mathbf{V}^\#(\varphi_{m_n}^{\text{az}}, \varphi_{m_n}^{\text{el}}) \mathbf{U}^\#(\phi_{m_n}^{\text{az}}, \phi_{m_n}^{\text{el}}) \right] [\tilde{\mathbf{U}}^{\text{el}} \otimes \tilde{\mathbf{U}}^{\text{az}}]^* \\ &= \sum_{n \in \mathcal{B}_{\text{FWV}}} \sum_{m=1}^{M_n} \beta_{m_n} \cdot e^{j[2\pi(\nu_{m_n} t - f \tau_{m_n}) + \Phi_{m_n}]} [\tilde{\mathbf{V}}^{\text{el}} \otimes \tilde{\mathbf{V}}^{\text{az}}]^H \\ &\quad [\mathbf{b}(\vartheta_{m_n}^{\text{el}}) \otimes \mathbf{a}(\vartheta_{m_n}^{\text{az}})] [\mathbf{b}(\theta_{m_n}^{\text{el}}) \otimes \mathbf{a}(\theta_{m_n}^{\text{az}})]^T [\tilde{\mathbf{U}}^{\text{el}} \otimes \tilde{\mathbf{U}}^{\text{az}}]^* \\ &= \sum_{n \in \mathcal{B}_{\text{FWV}}} \sum_{m=1}^{M_n} \beta_{m_n} \cdot e^{j[2\pi(\nu_{m_n} t - f \tau_{m_n}) + \Phi_{m_n}]} \\ &\quad \left[ (\tilde{\mathbf{V}}^{\text{el}})^H \mathbf{b}(\vartheta_{m_n}^{\text{el}}) \otimes (\tilde{\mathbf{V}}^{\text{az}})^H \mathbf{a}(\vartheta_{m_n}^{\text{az}}) \right] \end{aligned}$$

$$[\mathbf{b}^T(\theta_{m_n}^{\text{el}}) \tilde{\mathbf{U}}^{\text{el}*} \otimes \mathbf{a}^T(\theta_{m_n}^{\text{az}}) \tilde{\mathbf{U}}^{\text{az}*}] \quad (67)$$

$$\begin{aligned} \mathbf{H}_B^{\text{NWV}}(t, f) &= [\tilde{\mathbf{V}}^{\text{el}} \otimes \tilde{\mathbf{V}}^{\text{az}}]^H \mathbf{H}^{\text{NWV}}(t, f) [\tilde{\mathbf{U}}^{\text{el}} \otimes \tilde{\mathbf{U}}^{\text{az}}]^* \\ &= [\tilde{\mathbf{V}}^{\text{el}} \otimes \tilde{\mathbf{V}}^{\text{az}}]^H \left[ \sum_{n \in \mathcal{B}_{\text{NWV}}} \sum_{m=1}^{M_n} \beta_{m_n} \cdot e^{j[2\pi(\nu_{m_n} t - f \tau_{m_n}) + \Phi_{m_n}]} \right. \\ &\quad \left. \mathbf{V}^\#(\varphi_{m_n}^{\text{az}}, \varphi_{m_n}^{\text{el}}) \mathbf{U}_N^\#(\phi_{m_n}^{\text{az}}, \phi_{m_n}^{\text{el}}) \right] [\tilde{\mathbf{U}}^{\text{el}} \otimes \tilde{\mathbf{U}}^{\text{az}}]^* \\ &= \sum_{n \in \mathcal{B}_{\text{NWV}}} \sum_{m=1}^{M_n} \beta_{m_n} \cdot e^{j[2\pi(\nu_{m_n} t - f \tau_{m_n}) + \Phi_{m_n}]} [\tilde{\mathbf{V}}^{\text{el}} \otimes \tilde{\mathbf{V}}^{\text{az}}]^H \\ &\quad [\mathbf{b}(\vartheta_{m_n}^{\text{el}}) \otimes \mathbf{a}(\vartheta_{m_n}^{\text{az}})] [\mathbf{b}_N(\theta_{m_n}^{\text{el}}) \otimes \mathbf{a}_N(\theta_{m_n}^{\text{az}})]^T \\ &\quad \times [\tilde{\mathbf{U}}^{\text{el}} \otimes \tilde{\mathbf{U}}^{\text{az}}]^* \\ &= \sum_{n \in \mathcal{B}_{\text{FWV}}} \sum_{m=1}^{M_n} \beta_{m_n} \cdot e^{j[2\pi(\nu_{m_n} t - f \tau_{m_n}) + \Phi_{m_n}]} \\ &\quad \left[ (\tilde{\mathbf{V}}^{\text{el}})^H \mathbf{b}(\vartheta_{m_n}^{\text{el}}) \otimes (\tilde{\mathbf{V}}^{\text{az}})^H \mathbf{a}(\vartheta_{m_n}^{\text{az}}) \right] \\ &\quad [\mathbf{b}_N^T(\theta_{m_n}^{\text{el}}) \tilde{\mathbf{U}}^{\text{el}*} \otimes \mathbf{a}_N^T(\theta_{m_n}^{\text{az}}) \tilde{\mathbf{U}}^{\text{az}*}] \end{aligned} \quad (68)$$

$$\begin{aligned} \mathbf{H}_B^{\text{NPV}}(t, f) &= [\tilde{\mathbf{V}}^{\text{el}} \otimes \tilde{\mathbf{V}}^{\text{az}}]^H \mathbf{H}^{\text{NPV}}(t, f) [\tilde{\mathbf{U}}^{\text{el}} \otimes \tilde{\mathbf{U}}^{\text{az}}]^* \\ &= [\tilde{\mathbf{V}}^{\text{el}} \otimes \tilde{\mathbf{V}}^{\text{az}}]^H \left[ \sum_{n \in \mathcal{B}_{\text{NPV}}} \sum_{m=1}^{M_n} \beta_{m_n} \cdot e^{j[2\pi(\nu_{m_n} t - f \tau_{m_n}) + \Phi_{m_n}]} \right. \\ &\quad \left. \mathbf{V}^\#(\varphi_{m_n}^{\text{az}}, \varphi_{m_n}^{\text{el}}) \hat{\mathbf{U}}_N^\#(\phi_{m_n}^{\text{az}}, \phi_{m_n}^{\text{el}}) \right] [\tilde{\mathbf{U}}^{\text{el}} \otimes \tilde{\mathbf{U}}^{\text{az}}]^* \\ &= \sum_{n \in \mathcal{B}_{\text{FWV}}} \sum_{m=1}^{M_n} \beta_{m_n} \cdot e^{j[2\pi(\nu_{m_n} t - f \tau_{m_n}) + \Phi_{m_n}]} [\tilde{\mathbf{V}}^{\text{el}} \otimes \tilde{\mathbf{V}}^{\text{az}}]^H \\ &\quad [\mathbf{b}(\vartheta_{m_n}^{\text{el}}) \otimes \mathbf{a}(\vartheta_{m_n}^{\text{az}})] [\hat{\mathbf{b}}_N(\theta_{m_n}^{\text{el}}) \otimes \hat{\mathbf{a}}_N(\theta_{m_n}^{\text{az}})]^T \\ &\quad \times [\tilde{\mathbf{U}}^{\text{el}} \otimes \tilde{\mathbf{U}}^{\text{az}}]^* \\ &= \sum_{n \in \mathcal{B}_{\text{FWV}}} \sum_{m=1}^{M_n} \beta_{m_n} \cdot e^{j[2\pi(\nu_{m_n} t - f \tau_{m_n}) + \Phi_{m_n}]} \\ &\quad \left[ (\tilde{\mathbf{V}}^{\text{el}})^H \mathbf{b}(\vartheta_{m_n}^{\text{el}}) \otimes (\tilde{\mathbf{V}}^{\text{az}})^H \mathbf{a}(\vartheta_{m_n}^{\text{az}}) \right] \\ &\quad [\hat{\mathbf{b}}_N^T(\theta_{m_n}^{\text{el}}) \tilde{\mathbf{U}}^{\text{el}*} \otimes \hat{\mathbf{a}}_N^T(\theta_{m_n}^{\text{az}}) \tilde{\mathbf{U}}^{\text{az}*}]. \end{aligned} \quad (69)$$

The elements in  $\mathbf{H}_B^{\text{FWV}}(t, f)$ ,  $\mathbf{H}_B^{\text{NWV}}(t, f)$ , and  $\mathbf{H}_B^{\text{NPV}}(t, f)$  are calculated by

$$\begin{aligned} h_{B, p_v p_h, q_v q_h}^{\text{FWV}}(t, f) &= \sum_{n \in \mathcal{B}_{\text{FWV}}} \sum_{m=1}^{M_n} \beta_{m_n} \cdot e^{j[2\pi(\nu_{m_n} t - f \tau_{m_n}) + \Phi_{m_n}]} \\ &\quad \frac{1}{\sqrt{Q_v}} \sum_{\alpha=0}^{Q_v-1} e^{j2\pi\alpha(\vartheta_{m_n}^{\text{el}} - \tilde{\vartheta}_{q_v}^{\text{el}})} \frac{1}{\sqrt{Q_h}} \sum_{\beta=0}^{Q_h-1} e^{j2\pi\beta(\vartheta_{m_n}^{\text{az}} - \tilde{\vartheta}_{q_h}^{\text{az}})} \end{aligned}$$

$$\frac{1}{\sqrt{P_v}} \sum_{a=0}^{P_v-1} e^{j2\pi a(\theta_{m_n}^{el} - \tilde{\theta}_{p_v}^{el})} \frac{1}{\sqrt{P_h}} \sum_{b=0}^{P_h-1} e^{j2\pi b(\theta_{m_n}^{az} - \tilde{\theta}_{p_h}^{az})} \quad (70)$$

$$h_{B,p_v,p_h,q_v,q_h}^{NWV}(t, f) = \sum_{n \in \mathcal{B}_{NWV}} \sum_{m=1}^{M_n} \beta_{m_n} \cdot e^{j[2\pi(\nu_{m_n} t - f\tau_{m_n}) + \Phi_{m_n}]}$$

$$\frac{1}{\sqrt{Q_v}} \sum_{\alpha=0}^{Q_v-1} e^{j2\pi\alpha(\vartheta_{m_n}^{el} - \tilde{\vartheta}_{q_v}^{el})} \frac{1}{\sqrt{Q_h}} \sum_{\beta=0}^{Q_h-1} e^{j2\pi\beta(\vartheta_{m_n}^{az} - \tilde{\vartheta}_{q_h}^{az})}$$

$$\frac{1}{\sqrt{P_v}} \sum_{a=0}^{P_v-1} e^{j2\pi\left(\frac{(a-\delta^T+d-\theta)-a}{d-a-\delta^T} - a\tilde{\theta}_{p_v}^{el}\right)} \frac{1}{\sqrt{P_h}} \sum_{b=0}^{P_h-1} e^{j2\pi\left(\frac{d-b-\theta_{m_n}^{az}}{d-b-\delta^T} - b\tilde{\theta}_{p_h}^{az}\right)} \quad (71)$$

$$h_{B,p_v,p_h,q_v,q_h}^{NPV}(t, f) = \sum_{n \in \mathcal{B}_{NPV}} \sum_{m=1}^{M_n} \beta_{m_n} \cdot e^{j[2\pi(\nu_{m_n} t - f\tau_{m_n}) + \Phi_{m_n}]}$$

$$\frac{1}{\sqrt{Q_v}} \sum_{\alpha=0}^{Q_v-1} e^{j2\pi\alpha(\vartheta_{m_n}^{el} - \tilde{\vartheta}_{q_v}^{el})} \frac{1}{\sqrt{Q_h}} \sum_{\beta=0}^{Q_h-1} e^{j2\pi\beta(\vartheta_{m_n}^{az} - \tilde{\vartheta}_{q_h}^{az})}$$

$$\frac{1}{\sqrt{P_v}} \sum_{a=I_{s,n}^h-1}^{I_{e,n}^h-1} e^{j2\pi\left(\frac{(a-\delta^T+d-\theta)-a}{d-a-\delta^T} - a\tilde{\theta}_{p_v}^{el}\right)}$$

$$\frac{1}{\sqrt{P_h}} \sum_{b=I_{s,n}^v-1}^{I_{e,n}^v-1} e^{j2\pi\left(\frac{d-b-\theta_{m_n}^{az}}{d-b-\delta^T} - b\tilde{\theta}_{p_h}^{az}\right)} \quad (72)$$

## REFERENCES

- [1] X.-H. You et al., "Towards 6G wireless communication networks: Vision, enabling technologies, and new paradigm shifts," *Sci. China Inf. Sci.*, vol. 64, no. 1, Jan. 2021, Art. no. 110301, doi: [10.1007/s11432-020-2955-6](https://doi.org/10.1007/s11432-020-2955-6).
- [2] W. Jiang, B. Han, M. A. Habibi, and H. D. Schotten, "The road towards 6G: A comprehensive survey," *IEEE Open J. Commun. Soc.*, vol. 2, pp. 334–366, 2021.
- [3] S. Chen, Y.-C. Liang, S. Sun, S. Kang, W. Cheng, and M. Peng, "Vision, requirements, and technology trend of 6G: How to tackle the challenges of system coverage, capacity, user data-rate and movement speed," *IEEE Wireless Commun.*, vol. 27, no. 2, pp. 218–228, Apr. 2020.
- [4] W. Saad, M. Bennis, and M. Chen, "A vision of 6G wireless systems: Applications, trends, technologies, and open research problems," *IEEE Netw.*, vol. 34, no. 3, pp. 134–142, May/June 2020.
- [5] C. D. Alwis et al., "Survey on 6G frontiers: Trends, applications, requirements, technologies and future research," *IEEE Open J. Commun. Soc.*, vol. 2, pp. 836–886, 2021.
- [6] W. Hong et al., "The role of millimeter-wave technologies in 5G/6G wireless communications," *IEEE J. Microw.*, vol. 1, no. 1, pp. 101–122, Jan. 2021.
- [7] T. S. Rappaport et al., "Millimeter wave mobile communications for 5G cellular: It will work!," *IEEE Access*, vol. 1, pp. 335–349, 2013.
- [8] T. S. Rappaport, Y. Xing, G. R. MacCartney, A. F. Molisch, E. Mellios, and J. Zhang, "Overview of millimeter wave communications for fifth-generation (5G) wireless networks—with a focus on propagation models," *IEEE Trans. Antennas Propag.*, vol. 65, no. 12, pp. 6213–6230, Dec. 2017.
- [9] T. S. Rappaport et al., "Wireless communications and applications above 100 GHz: Opportunities and challenges for 6G and beyond," *IEEE Access*, vol. 7, pp. 78729–78757, 2019.
- [10] C.-X. Wang, J. Wang, S. Hu, Z. Jiang, J. Tao, and F. Yan, "Key technologies in 6G THz wireless communication systems: A survey," *IEEE Veh. Technol. Mag.*, vol. 16, no. 4, pp. 27–37, Dec. 2021.
- [11] M. Polese, J. M. Jornet, T. Melodia, and M. Zorzi, "Toward end-to-end, full-stack 6G terahertz networks," *IEEE Commun. Mag.*, vol. 58, no. 11, pp. 48–54, Nov. 2020.
- [12] C.-X. Wang, J. Bian, J. Sun, W. Zhang, and M. Zhang, "A survey of 5G channel measurements and models," *IEEE Commun. Surv. Tuts.*, vol. 20, no. 4, pp. 3142–3168, Fourthquarter 2018.
- [13] S. Priebe, M. Kannicht, M. Jacob, and T. Kürner, "Ultra broadband indoor channel measurements and calibrated ray tracing propagation modeling at THz frequencies," *J. Commun. Netw.*, vol. 15, no. 6, pp. 547–558, Dec. 2013.
- [14] P. Tang et al., "Channel measurement and path loss modeling from 220 GHz to 330 GHz for 6G wireless communications," *China Commun.*, vol. 18, no. 5, pp. 19–32, May 2021.
- [15] J. He, Y. Chen, Y. Wang, Z. Yu, and C. Han, "Channel measurement and path-loss characterization for low-terahertz indoor scenarios," in *Proc. IEEE Int. Conf. Commun. Workshops*, 2021, pp. 1–6.
- [16] V. Petrov, M. Komarov, D. Moltchanov, J. M. Jornet, and Y. Koucheryavy, "Interference and SINR in millimeter wave and terahertz communication systems with blocking and directional antennas," *IEEE Trans. Wireless Commun.*, vol. 16, no. 3, pp. 1791–1808, Mar. 2017.
- [17] J. Sun, F. Hu, and S. Lucyszyn, "Predicting atmospheric attenuation under pristine conditions between 0.1 and 100 THz," *IEEE Access*, vol. 4, pp. 9377–9399, 2016.
- [18] Q. Jing and D. Liu, "Study of atmospheric attenuation characteristics of terahertz wave based on line-by-line integration," *Int. J. Commun. Syst.*, vol. 31, no. 12, pp. 1–16, 2018.
- [19] J. Wang et al., "A novel 3D non-stationary GBSM for 6G THz ultra massive MIMO wireless systems," *IEEE Trans. Veh. Technol.*, vol. 70, no. 12, pp. 12312–12324, Dec. 2021.
- [20] C. Jansen et al., "Diffuse scattering from rough surfaces in THz communication channels," *IEEE Trans. THz Sci. Technol.*, vol. 1, no. 2, pp. 462–472, Nov. 2011.
- [21] J. Kokkonen, V. Petrov, D. Moltchanov, J. Lehtomaeki, Y. Koucheryavy, and M. Juntti, "Wideband terahertz band reflection and diffuse scattering measurements for beyond 5G indoor wireless networks," in *Proc. Eur. Wireless; 22th Eur. Wireless Conf.*, 2016, pp. 1–6.
- [22] F. Sheikh, Y. Gao, and T. Kaiser, "A study of diffuse scattering in massive MIMO channels at terahertz frequencies," *IEEE Trans. Antennas Propag.*, vol. 68, no. 2, pp. 997–1008, Feb. 2020.
- [23] "Study on channel model for frequencies from 0.5 to 100 GHz, Version 15.0.0," 3rd Generation Partnership Project, Sophia Antipolis, France, Tech. Rep. 38.901, Jun. 2018.
- [24] *IMT Vision-Framework and Overall Objectives of the Future Development of IMT for 2020 and Beyond*, ITU-R Standard M.2412-0, Oct. 2017.
- [25] S. Priebe and T. Kürner, "Stochastic modeling of THz indoor radio channels," *IEEE Trans. Wireless Commun.*, vol. 12, no. 9, pp. 4445–4455, Sep. 2013.
- [26] S. Priebe, M. Jacob, and T. Kürner, "Angular and RMS delay spread modeling in view of THz indoor communication systems," *Radio Sci.*, vol. 49, pp. 242–251, Mar. 2014.
- [27] C. Han, A. O. Bicen, and I. F. Akyildiz, "Multi-ray channel modeling and wideband characterization for wireless communications in the terahertz band," *IEEE Trans. Wireless Commun.*, vol. 14, no. 5, pp. 2402–2412, May 2015.
- [28] Y. Zhang, L. Zhao, and Z. He, "A 3-D hybrid dynamic channel model for indoor THz communications," *China Commun.*, vol. 18, no. 5, pp. 50–65, May 2021.
- [29] I. Akyildiz and J. M. Jornet, "Realizing ultra-massive MIMO (1024) communication in the (0.06–10) terahertz band," *Nano Commun. Netw.*, vol. 8, pp. 46–54, May 2016.
- [30] C. Han, J. M. Jornet, and I. Akyildiz, "Ultra-massive MIMO channel modeling for graphene-enabled terahertz-band communications," in *Proc. IEEE 87th Veh. Technol. Conf.*, 2018, pp. 1–5.
- [31] Y. Yuan et al., "A 3D geometry-based THz channel model for 6G ultra massive MIMO systems," *IEEE Trans. Veh. Technol.*, vol. 71, no. 3, pp. 2251–2266, Mar. 2022.
- [32] S. Tarboush et al., "TeraMIMO: A channel simulator for wideband ultra-massive MIMO terahertz communications," *IEEE Trans. Veh. Technol.*, vol. 70, no. 12, pp. 12325–12341, Dec. 2021.
- [33] A. Brighente, M. Cerutti, M. Nicoli, S. Tomasin, and U. Spagnolini, "Estimation of wideband dynamic mmWave and THz channels for 5G systems and beyond," *IEEE J. Sel. Areas Commun.*, vol. 38, no. 9, pp. 2026–2040, Sep. 2020.

- [34] H. Sardeddeen, M.-S. Alouini, and T. Y. Al-Naffouri, "Terahertz-band ultra-massive spatial modulation MIMO," *IEEE J. Sel. Areas Commun.*, vol. 37, no. 9, pp. 2040–2052, Sep. 2019.
- [35] A. M. Elbir, K. V. Mishra, and S. Chatzinotas, "Terahertz-band joint ultra-massive MIMO radar-communications: Model-based and model-free hybrid beamforming," *IEEE J. Sel. Topics Signal Process.*, vol. 15, no. 6, pp. 1468–1483, Nov. 2021.
- [36] V. Jamali, A. M. Tulino, G. Fischer, R. R. Müller, and R. Schober, "Intelligent surface-aided transmitter architectures for millimeter-wave ultra massive MIMO systems," *IEEE Open J. Commun. Soc.*, vol. 2, pp. 144–167, 2021.
- [37] L. Bai, Z. Huang, Y. Li, and X. Cheng, "A 3D cluster-based channel model for 5G and beyond vehicle-to-vehicle massive MIMO channels," *IEEE Trans. Veh. Technol.*, vol. 70, no. 9, pp. 8401–8414, Sep. 2021.
- [38] J. Wang, C.-X. Wang, J. Huang, H. Wang, and X. Gao, "A general 3D space-time-frequency non-stationary THz channel model for 6G ultra massive MIMO wireless communication systems," *IEEE J. Sel. Areas Commun.*, vol. 39, no. 6, pp. 1576–1589, Jun. 2021.
- [39] J. Bian, C.-X. Wang, X. Gao, X. You, and M. Zhang, "A general 3D non-stationary wireless channel model for 5G and beyond," *IEEE Trans. Wireless Commun.*, vol. 20, no. 5, pp. 3211–3224, May 2021.
- [40] C.-X. Wang, Z. Lv, X. Gao, X.-H. You, Y. Hao, and H. Haas, "Pervasive channel modeling theory and applications to 6G GBSMs for all frequency bands and all scenarios," *IEEE Trans. Veh. Technol.*, vol. 71, no. 9, pp. 9159–9173, Sep. 2022.
- [41] Z. Wan, Z. Gao, F. Gao, M. D. Renzo, and M.-S. Alouini, "Terahertz massive MIMO with holographic reconfigurable intelligent surfaces," *IEEE Trans. Commun.*, vol. 69, no. 7, pp. 4732–4750, Jul. 2021.
- [42] C. Huang et al., "Multi-hop RIS-empowered terahertz communications: A DRL-based hybrid beamforming design," *IEEE J. Sel. Areas Commun.*, vol. 39, no. 6, pp. 1663–1677, Jun. 2021.
- [43] W. Yan et al., "Beamforming analysis and design for wideband THz reconfigurable intelligent surface communications," 2022, *arXiv:2207.11926*.
- [44] A. M. Sayeed, "Deconstructing multiantenna fading channels," *IEEE Trans. Signal Process.*, vol. 50, no. 10, pp. 2563–2579, Oct. 2002.
- [45] C. Sun, X. Gao, S. Jin, M. Matthaiou, Z. Ding, and C. Xiao, "Beam division multiple access transmission for massive MIMO communications," *IEEE Trans. Commun.*, vol. 63, no. 6, pp. 2170–2184, Jun. 2015.
- [46] L. You, X. Gao, G. Y. Li, X. -G. Xia, and N. Ma, "BDMA for millimeter-wave/terahertz massive MIMO transmission with per-beam synchronization," *IEEE J. Sel. Areas Commun.*, vol. 35, no. 7, pp. 1550–1563, Jul. 2017.
- [47] X. Shao, X. Chen, C. Zhong, and Z. Zhang, "Exploiting simultaneous low-rank and sparsity in delay-angular domain for millimeter-wave/terahertz wideband massive access," *IEEE Trans. Wireless Commun.*, vol. 21, no. 4, pp. 2336–2351, Apr. 2022.
- [48] Z. Zhang, Y. Xu, J. Yang, X. Li, and D. Zhang, "A survey of sparse representation: Algorithms and applications," *IEEE Access*, vol. 3, pp. 490–530, 2015.
- [49] F. Lai, C.-X. Wang, J. Huang, X. Gao, and F.-C. Zheng, "A novel beam domain channel model for B5G massive MIMO wireless communication systems," *IEEE Trans. Veh. Technol.*, vol. 72, no. 4, pp. 4143–4156, Apr. 2023.
- [50] J. Bian et al., "A novel 3D beam domain channel model for massive MIMO communication systems," *IEEE Trans. Wireless Commun.*, vol. 22, no. 3, pp. 1618–1632, Mar. 2023.
- [51] R. Feng, C.-X. Wang, J. Huang, and X. Gao, "Recent advances of ultramassive multiple-input, multiple-output technologies: Realizing a sixth-generation future in spatial and beam domains," *IEEE Veh. Technol. Mag.*, vol. 18, no. 1, pp. 70–79, Mar. 2023.
- [52] N. Czink, P. Cera, J. Salo, E. Bonek, J.-P. Nuutinen, and J. Ylitalo, "Improving clustering performance using multipath component distance," *Electron. Lett.*, vol. 42, no. 2, pp. 33–35, Jan. 2006.
- [53] P. Kyösti et al., "WINNER II channel models," IST-4-027756, WINNER II D1.1.2, v1.2, Apr. 2008.
- [54] X. Gao, L. Dai, and A. M. Sayeed, "Low RF-complexity technologies to enable millimeter-wave MIMO with large antenna array for 5G wireless communications," *IEEE Commun. Mag.*, vol. 56, no. 4, pp. 211–217, Apr. 2018.
- [55] T. Xie, L. Dai, D. W. K. Ng, and C.-B. Chae, "On the power leakage problem in millimeter-wave massive MIMO with lens antenna arrays," *IEEE Trans. Signal Process.*, vol. 67, no. 18, pp. 4730–4744, Sep. 2019.



**Jun Wang** (Student Member, IEEE) received the B.E. degree in information engineering in 2016 from Southeast University, Nanjing, China, where he is currently working toward the Ph.D. degree with the National Mobile Communications Research Laboratory. His research interests include THz wireless channel measurements and modeling.



**Cheng-Xiang Wang** (Fellow, IEEE) received the B.Sc. and M.Eng. degrees in communication and information systems from Shandong University, Jinan, China, in 1997 and 2000, respectively, and the Ph.D. degree in wireless communications from Aalborg University, Aalborg, Denmark, in 2004.

He was a Research Assistant with the Hamburg University of Technology, Hamburg, Germany, from 2000 to 2001, a Visiting Researcher with Siemens AG Mobile Phones, Munich, Germany, in 2004, and a Research Fellow with the University of Agder, Grimstad, Norway, from 2001 to 2005. He has been with Heriot-Watt University, Edinburgh, U.K., since 2005, where he was promoted to a Professor in 2011. In 2018, he joined Southeast University, Nanjing, China, as a Professor. He is also a part-time Professor with Purple Mountain Laboratories, Nanjing. He has authored four books, three book chapters, and more than 500 papers in refereed journals and conference proceedings, including 27 highly cited papers. He has also delivered 24 invited keynote speeches/talks and 16 tutorials in international conferences. His research interests include wireless channel measurements and modeling, 6G wireless communication networks, and electromagnetic information theory.

Dr. Wang is a Member of the Academia Europaea (The Academy of Europe), a Member of the European Academy of Sciences and Arts (EASA), a Fellow of the Royal Society of Edinburgh (FRSE), IET, and China Institute of Communications (CIC), an IEEE Communications Society Distinguished Lecturer in 2019 and 2020, a Highly-Cited Researcher recognized by Clarivate Analytics in 2017–2020, and one of the most cited Chinese Researchers recognized by Elsevier in 2021. He is currently an Executive Editorial Committee Member of the IEEE TRANSACTIONS ON WIRELESS COMMUNICATIONS. He was the Editor of over ten international journals, including the IEEE TRANSACTIONS ON WIRELESS COMMUNICATIONS, from 2007 to 2009, the IEEE TRANSACTIONS ON VEHICULAR TECHNOLOGY, from 2011 to 2017, and the IEEE Transactions on Communications, from 2015 to 2017. He was the Guest Editor of the IEEE JOURNAL ON SELECTED AREAS IN COMMUNICATIONS, Special Issue on Vehicular Communications and Networks (Lead Guest Editor), Special Issue on Spectrum and Energy Efficient Design of Wireless Communication Networks, and Special Issue on Airborne Communication Networks. He was also the Guest Editor of the IEEE TRANSACTIONS ON BIG DATA, Special Issue on Wireless Big Data, and is the Guest Editor of the IEEE TRANSACTIONS ON COGNITIVE COMMUNICATIONS AND NETWORKING, Special Issue on Intelligent Resource Management for 5G and Beyond. He was the TPC Member, TPC Chair, and the General Chair for more than 80 international conferences. He was the recipient of 15 Best Paper Awards from IEEE GLOBECOM 2010, IEEE ICCT 2011, ITST 2012, IEEE VTC 2013Fall, IWCMC 2015, IWCMC 2016, IEEE/CIC ICC 2016, WPMC 2016, WOCC 2019, IWCMC 2020, WCSP 2020, CSPS2021, WCSP 2021, and IEEE/CIC ICC 2022. He also was the recipient of the 2020–2022 AI 2000 Most Influential Scholar Award Honorable Mention in recognition of his outstanding and vibrant contributions in the field of Internet of Things.



**Jie Huang** (Member, IEEE) received the B.E. degree in information engineering from Xidian University, Xi'an, China, in 2013, and the Ph.D. degree in information and communication engineering from Shandong University, Jinan, China, in 2018. From October 2018 to October 2020, he was a Postdoctoral Research Associate with the National Mobile Communications Research Laboratory, Southeast University, Nanjing, China, supported by the National Postdoctoral Program for Innovative Talents. From January 2019 to February 2020, he was a Postdoctoral Research Associate with Durham University, Durham, U.K. Since March 2019, he is a part-time Researcher with Purple Mountain Laboratories, China. Since November 2020, he has been an Associate Professor with the National Mobile Communications Research Laboratory, Southeast University. He has authored and coauthored more than 70 papers in refereed journals and conference proceedings. His research interests include millimeter wave, massive MIMO, reconfigurable intelligent surface channel measurements and modeling, wireless Big Data, and 6G wireless communications. He was the recipient of the Best Paper Awards from WPMC 2016, WCSP 2020, and WCSP 2021. He has delivered eight tutorials in IEEE/CIC ICC 2021, IEEE PIMRC 2021, IEEE ICC 2022, IEEE VTC-Spring 2022, IEEE/CIC ICC 2022, IEEE VTC-Fall 2022, IEEE PIMRC 2022, and IEEE Globecom 2022.

Since March 2019, he is a part-time Researcher with Purple Mountain Laboratories, China. Since November 2020, he has been an Associate Professor with the National Mobile Communications Research Laboratory, Southeast University. He has authored and coauthored more than 70 papers in refereed journals and conference proceedings. His research interests include millimeter wave, massive MIMO, reconfigurable intelligent surface channel measurements and modeling, wireless Big Data, and 6G wireless communications. He was the recipient of the Best Paper Awards from WPMC 2016, WCSP 2020, and WCSP 2021. He has delivered eight tutorials in IEEE/CIC ICC 2021, IEEE PIMRC 2021, IEEE ICC 2022, IEEE VTC-Spring 2022, IEEE/CIC ICC 2022, IEEE VTC-Fall 2022, IEEE PIMRC 2022, and IEEE Globecom 2022.



**Rui Feng** (Member, IEEE) received the B.Sc. degree in communication engineering from Yantai University, Yantai, China, in 2011, the M.Eng. degree in signal and information processing from Yantai University, in 2014, and the Ph.D. degree in communication and information system from Shandong University, Jinan, China, in 2018. From July 2018 to September 2020, she was a lecture with Ludong University, Yantai, China. She is currently a Postdoctoral Research Associate with Purple Mountain Laboratories and Southeast University, Nanjing, China. Her research

interests include (ultra-) massive MIMO channel modeling theory and beam domain channel modeling.



**El-Hadi M. Aggoune** (Life Senior Member, IEEE) received the M.S. and Ph.D. degrees in electrical engineering from the University of Washington, Seattle, WA, USA. He was with several universities in the U.S. and abroad at many academic ranks including Endowed Chair Professor. He is listed as Inventor in several patents, one of them assigned to the Boeing Company, USA. He is a Professional Engineer registered with the state of Washington. He is currently a Professor and the Director of the Sensor Networks and Cellular Systems (SNCS) Research Center, University of Tabuk, Tabuk, Saudi Arabia. He coauthored papers in IEEE and other journals and conferences, and served on editorial boards and technical committees for many of them. His research interests include wireless communication, sensor networks, power systems, neurocomputing, and scientific visualization. He was the recipient of the IEEE Professor of the Year Award, UW. He was the Director of a Laboratory that was the recipient of the Boeing Supplier Excellence Award.

He was the recipient of the IEEE Professor of the Year Award, UW. He was the Director of a Laboratory that was the recipient of the Boeing Supplier Excellence Award.



**Yunfei Chen** (Senior Member, IEEE) received the B.E. and M.E. degrees in electronics engineering from Shanghai Jiaotong University, Shanghai, China, in 1998 and 2001, respectively, and the Ph.D. degree from the University of Alberta, Edmonton, AB, Canada, in 2006. He is currently a Professor with the Department of Engineering, University of Durham, Durham, U.K. His research interests include wireless communications, performance analysis, joint radar communications designs, cognitive radios, wireless relaying and energy harvesting.